CO Oxidation on the $Au_{15}Cu_{15}$ Cluster and the Role of Vacancies in the MgO(100) Support

Li Ma,[†,‡,§] Marko Melander,[§,¶] Timo Weckman,[§] Kari Laasonen,[§] and Jaakko Akola*[,†,‡]

[‡]Department of Physics, Tampere University of Technology, FI-33101 Tampere, Finland

[†]COMP Centre of Excellence, Department of Applied Physics, Aalto University, FI-00076 Aalto, Finland

[§]COMP Centre of Excellence, Department of Chemistry, Aalto University, FI-00076 Aalto, Finland

[¶]Department of Energy Conversion and Storage, Technical University of Denmark, DK-4000 Roskilde, Denmark

ABSTRACT

A comprehensive theoretical study of an $Au_{15}Cu_{15}$ cluster on MgO(100) supports and its catalytic activity for CO oxidation has been performed based on the density functional theory and microkinetic modeling. Molecular adsorption and different reaction paths based on the Langmuir−Hinshelwood (LH) and Eley−Rideal (ER) mechanisms have been explored by tuning the location of vacancies in MgO(100). The charge states of the $Au_{15}Cu_{15}$ cluster are negative on all supports, defect-free, O-vacancy (F-center) and Mg-vacancy (V-center), and the effect is significantly amplified on the F-center. In each case, the O_2 molecule can be effectively activated upon adsorption and dissociated to 2×O atoms easily, and the reaction modeling takes into account also the reaction paths with adsorbed O atoms. Overall, CO oxidation has lower reaction barriers on the cluster on the F-center. The microkinetic modeling analysis reveals that CO oxidation is very sensitive to the CO partial pressure, as the relatively strong CO binding leads readily to CO poisoning of the cluster surface sites and hinders CO_2 formation. For low CO partial pressures, the catalytic reaction takes place already at 150 K for the cluster on the F-center. The CO_2 production rates are much lower for the defect-free and V-center supports which display similar increased activity at elevated temperatures. In all cases, the right combination of CO and O_2 partial pressures is instrumental for CO_2 production.

1. INTRODUCTION

Oxidation of CO to CO_2 using gold nanoparticles as catalysts has been a topic of great interest since the work of Haruta *et al.* in 1987.[1] Comprehensive experimental and computational studies have been carried out to reveal the fundamental mechanisms for high catalytic activity, including the exploration of the role of the oxide support, the most active sites on oxide-supported gold nanoparticles, as well as the size- and shape-dependence of the nanoparticles.[2-10] Up to now, several factors have been discussed in relation to the high catalytic activity of Au nanoparticles on supports,[11-14] for example, the chemical structure of support, charge transfer between the nanoparticle and support, and perimeter sites at the support interface. Specifically, the charge transfer between a gold cluster and support depends strongly on the atomic structure and chemistry at the interface.[15-17]

Experiments have shown the presence of positively charged gold sites result in the formation of AuO_x or AuO(OH) phases in supported catalysts, such as in $Au/Mg(OH)_2$,[18] Au/MgO,[19-20] Au/CeO_2,[21] Au/TiO_2,[22] and $Au/\alpha\text{-}Fe_2O_3$[23] systems, and these phases are important for CO oxidation. On the other hand, negatively charged Au clusters can exist on supports with defects.[24-25] For instance, the oxygen-vacancy (F-center) defects present on MgO surfaces were suggested to cause charge transfer to supported Au_8 clusters.[9] The negatively charged Au_8 clusters were capable of catalyzing CO oxidation at temperatures as low as 140 K. In comparison, clusters on the defect-free MgO surface were much less active.

More recently, Stamatakis *et al.*[17] performed density functional theory (DFT) calculations with kinetic Monte Carlo simulations and found a complex behavior for CO oxidation, which depends on support-induced charge states that are induced by support vacancies. The investigated Au_6 clusters are neutral and positive, respectively, depending whether they have been positioned on a clean MgO surface or an Mg vacancy, and O_2 does not bind strongly enough to the clusters, while CO poisons the catalyst. On the other hand, O_2 binds stronger (chemisorbs) on negatively charged Au_6 clusters

as a result of the charge gained from F-centers. Here, the active catalyst eventually deactivates due to CO_3 (carbonate) accumulations via an unusual catalyst "breathing" mechanism (restructuring).

While there is an immense interest in supported (elemental) gold nanoparticles, the use of nanoalloys as catalysts is developing fast since they enable fine-tuning the catalytic properties of metals by chemical composition. Gold and copper have had many uses in catalysis for a long time,[26] and their combination enables to reduce the cost of gold and ameliorate the instability of copper. Gold, silver and copper form alloys very easily since they have the same face-centered cubic (fcc) crystal structure and similar lattice spacing. Three ordered alloys exist for the AuCu system in bulk crystals: $Au_{0.5}Cu_{0.5}$ (fcc, L_{10}), $Au_{0.25}Cu_{0.75}$ and $Au_{0.75}Cu_{0.25}$ (both fcc, L_{12}). The reproduction of the stoichiometric bulk alloys for AuCu clusters has been achieved in experiments.[26] For example, Pauwels *et al.*[27] reported the generation of AuCu clusters on amorphous carbon and MgO substrates by laser vaporization and deposited at low energy. Several geometrical motifs such as cuboctahedra, decahedra and various quasi-spherical geometrical structures were observed on carbon substrate. The truncated octahedral morphology was the only one observed on MgO substrate. All the clusters with the stoichiometric compositions $Au_{0.25}Cu_{0.75}$, $Au_{0.5}Cu_{0.5}$ and $Au_{0.75}Cu_{0.25}$ exhibit fcc structures and a cube-on-cube epitaxy relation with the MgO(100) substrate. From the computational point of view, Ferrando and co-workers[28] searched the structures of AuCu clusters adsorbed on MgO(100). The fcc pyramids and five-fold daisy structures were found to be close in total energy for the AuCu cluster of 30 atoms. For 40 and 50 atoms, icosahedral isomers prevailed.

The motivation of our theoretical study stems from a recent review by Hutchings and co-workers where the importance of AuCu alloy in catalysis was addressed.[26] So far, studies on AuCu clusters have focused on nanoparticle synthesis and characterization as well as fundamental investigations to understand the properties of nanoalloy particles.[26,29] There are only few investigations on catalysis, and they have been limited to the oxidation of CO,[30-33] benzyl alcohol[34] and propene on supported AuCu nanoparticles.[35-37] For CO oxidation, it has been shown that AuCu catalysts are more active

than elemental gold or copper catalysts, and that the temperature for CO conversion is lowered.[30-31] This has been described in terms of a synergistic interaction between Au and Cu, which increases the catalytic activity. In this article, we use DFT calculations combined with microkinetic model simulations to reveal the CO oxidation reaction mechanism on an MgO-supported $Au_{15}Cu_{15}$ cluster with a pyramidal shape (fcc). We elucidate the role of vacancies in the MgO support and their effects in the cluster structure/shape and charge states.

2. COMPUTATIONAL DETAILS

2.1. DFT Calculations

The DFT calculations were carried out using the spin-polarized, generalized gradient approximation of the exchange-correlation energy and the functional form by Perdew-Burke-Ernzerhof (GGA-PBE)[38] as implemented in the CP2K program package.[39,40] The Kohn-Sham orbitals and electron density were represented by Gaussian and plane wave (GPW) basis sets. For the Gaussian expansion of the wave functions, a molecularly-optimized double-zeta valence plus polarization (DZVP) basis set was used, where the basis set superposition error (BSSE) has been reduced by construction.[41] The additional complementary plane wave basis set with a 600 Ry kinetic energy cutoff was used for describing electron density, and the interaction between valence electrons and ions (nuclei + core electrons) was based on the analytical pseudopotentials by Goedecker, Teter, and Hutter (GTH).[42]

A 6×6 MgO(100) slab model with four atomic layers (288 atoms) and a vacuum layer of 20 Å was prepared for the MgO support, which is sufficient to describe the energetics of the oxidation catalysis by MgO-supported AuCu clusters.[28,43] The two lower layers of the substrate were held fixed at the optimal DFT lattice constant of 4.24 Å, which is in agreement with the experimental lattice constant of 4.22 Å.[43] An fcc pyramidal structure of the $Au_{15}Cu_{15}$ cluster, which has been characterized in previous studies,[27,28] was chosen as a model of the AuCu particle on MgO(100).

Ferrando and co-workers[28] found that the daisy structure competes with the fcc structure by only 0.07 eV higher total energy. We re-optimized these two structures by the present computational scheme and found that the fcc structure is 0.75 eV more favorable than the daisy structure. All the molecular adsorption calculations were done at the low coverage limit, so that only few molecule and/or atoms were considered. The higher coverages would result in an enormous number of configurations and such computations are not feasible in this context.

Bader algorithm was used to analyze the spatial charge decomposition among constituent atoms.[44] The Climbing Image Nudged Elastic Band (CI-NEB) method was applied for mapping the reaction paths.[45] The vibrational analysis was performed to further identify the obtained minima and transition states structures. Zero-point energy (ZPE) corrections were systematically included in the energy calculations. Furthermore, our previous benchmarks for CO oxidation on Cu clusters with hybrid DFT functionals (PBE0 and B3LYP) (Ref. 46) have shown that while the reaction barriers are somewhat lower for GGA-PBE, the energetic ordering of different reactions paths (barriers) remains the same.

2.2. Microkinetic Modeling

Microkinetic modeling was used to investigate catalytic reaction systems according to elementary reactions and their interrelations. The technique does not require any prior assumptions about the rate-determining steps or surface coverages of intermediates in the reactions. In this way, the rate expressions can use measured and/or estimated physical and chemical parameters for modeling reactions.[47]

For the surface reactions, the forward rate constant ($k_{f,i}$) was calculated for each reaction step using the harmonically approximated Eyring equation[48] based on the transition-state theory:

$$k_{f,i} = \frac{k_B T}{h} e^{-\frac{\Delta G_i^{\dagger}}{k_B T}} \quad (1)$$

where k_B is the Boltzmann's constant, h is the Planck's constant, T is the absolute temperature, and $\Delta G_i^{\dagger}$ is the Gibbs activation free energy for the reaction pathway i. The reverse rate constant ($k_{r,i}$)

was calculated correspondingly. From the forward and reverse rate constants, the thermodynamic equilibrium constant K_i was calculated as

$$K_i = \frac{k_{f,i}}{k_{r,i}} = e^{-\frac{\Delta G_i^{\ddagger}}{k_B T}} \quad (2)$$

where $\Delta G_i^{\ddagger}$ is the Gibbs free energy of reaction.

The ideal gas limit was used to estimate the free energies. The difference of Gibbs free energy between two states was calculated as[48]

$$\Delta G = \Delta(E_{elec} + E_{ZPE}) - T\Delta S \quad (3)$$

where E_{elec} is the electronic and E_{ZPE} is the zero-point energy of a configuration (state). ΔS is the change in entropy between the two states. For immobile adsorbed species, bond vibrations were treated as harmonic oscillations, whereas for the gaseous molecules, translational and rotational modes contributions were also included.

In addition, the particle flux from the kinetic gas theory[48] was used to express the forward rate for a non-activated unimolecular adsorption process:

$$k_{f,i} = \frac{P\sigma(T,\theta)}{\sqrt{2\pi m k_B T}} A_i \quad (4)$$

where the P is the pressure of the adsorbant, m is mass of the precursor molecule and A_i is the area of the adsorption site i. The adsorption site area was considered to be equal to the area of the adjacent triangle for O_2 molecule adsorption (bridge site). For CO molecule adsorption (top site), it is one third of the area of the adjacent triangle. $\sigma(T,\theta)$ is the sticking probability of the adsorbant, which was estimated to be temperature-independent and approximated as the fractional coverage of the free adsorption sites (see Supporting Information). The initial sticking coefficient of one is assumed for O_2 and CO adsorption. The previous studies show that CO adsorbs non-dissociatively on Au surfaces with high initial sticking probability.[49,50] For oxygen adsorption on Cu(100),[51] the sticking coefficient of the incoming O_2 molecules is low at small energies, which has been

interpreted as an indication of the existence of a small dissociation barrier for the O_2 dissociation at the clean Cu(100) surface. Our calculation (below) of O_2 dissociation is consistent with this finding.

For the sake of thermodynamic consistency, the reverse rate constant is again given as

$$k_{r,i} = \frac{k_{f,i}}{K_i} \tag{5}$$

After defining the forward and reverse rate constants (above), the surface coverages of the possible reaction intermediates and the fraction of free sites were obtained from the solution of the full set of steady-state rate equations (see Supporting Information).

3. RESULTS AND DISCUSSION

3.1. $Au_{15}Cu_{15}$ on MgO Supports

The interaction between the AuCu cluster and the oxide support plays an important role in the cluster properties and strongly affects its catalytic activity. Thus, we first investigated the structural behavior and the nature of support/cluster interaction of the $Au_{15}Cu_{15}$ cluster on MgO(100) before examining the catalytic mechanisms. To illustrate how the support vacancies influence the morphology and nature of the AuCu cluster, we considered three cases: an ideal MgO support, MgO support having an O-vacancy (F-center), and MgO support with an Mg-vacancy (V-center) on the surface. An F-center or a V-center can be created by removing an O atom or an Mg atom from the surface. For the sake of consistency, we have considered the same pyramidal (fcc) cluster geometry as the starting point for each case, while we cannot completely rule out the existence of other structural low-energy motifs for the $Au_{15}Cu_{15}$ cluster on supports with defects.

Different point defects sites exist for the vacancies with respect to the adsorption of $Au_{15}Cu_{15}$ on MgO(100). Here, we examined the different vacancy sites to locate the energetically most favorable adsorption configurations. The adsorption energies of $Au_{15}Cu_{15}$ clusters (E_{ad}^1) on MgO(100) supports were computed as:

$$E_{ad}^1 = E(Au_{15}Cu_{15}) + E(MgO) - E(Au_{15}Cu_{15}/MgO) \tag{6}$$

where $E(X)$ is the total energy of the corresponding system X.

In Figure 1, we show the most stable adsorption geometries of $Au_{15}Cu_{15}$ clusters on MgO(100) supports and the corresponding MgO(100) surfaces with assigned point defects sites. The adsorption energy, geometric parameters, and charge transfer between $Au_{15}Cu_{15}$ and MgO(100) are listed in Table 1. We see for the three supports that the adsorption geometries of $Au_{15}Cu_{15}$ are different. On the defect-free MgO surface [Figure 1(a-d)], the $Au_{15}Cu_{15}$ cluster is an fcc pyramidal structure (C_{2v}) with Au-O and Cu-O bonds between the AuCu/MgO interface. The Au-Au, Cu-Cu, and Au-Cu bond lengths of the cluster are in the range of 2.70-2.78 Å, 2.44-2.94 Å, and 2.60-2.88 Å, respectively. The shape of the bottom layer of the cluster is a square with 12 Au atoms on the periphery and 4 Cu atoms on the center. Upon adsorption, the Cu atoms directly above support O atoms move down forming Cu-O bonds in the range of 2.07-2.09 Å, which are considerably shorter than the Au-O bond lengths (2.66-3.10 Å). According to the Bader charge analysis, the cluster carries a negative net charge of -1.96 e, which indicates that the MgO(100) surface has transferred charge (electrons) to the $Au_{15}Cu_{15}$ cluster. Compared with the previous reports on Au/MgO(100) systems, different charge transfers are reported. For example, Au_6 cluster is almost neutral on an ideal support, attracting a negligible electron density (-0.2 e).[17] Au_8 is also not charged on MgO(100).[9] However, electron charge transfer has been reported to Au_1, Au_2 and Au_{10}.[52] Here, a detailed analysis of the atomic charges shows that all Au atoms in the AuCu cluster gain electron density up to 0.4 e, each. On the contrary, Cu atoms lose electron density up to 0.3 e, each, except the one located in the interior site of the pyramidal cage. This site is screened by the surrounding metal atoms which results in almost no charge transfer.

On defected MgO surfaces, the F-center causes geometric change to the supported $Au_{15}Cu_{15}$ cluster (C_s) [Figure 1(e-f)], primarily by the downward movement a single Au atom. Figure 1(e) shows how the corner Au atom tilts towards the F-center but does not move deeper into the vacancy (distance from the vacancy site is 1.69 Å). The rest of the Au atoms at the interface form Au-O

bonds with the range of 2.68-3.12 Å, which are longer than the Cu-O bond lengths (2.16-2.25 Å). The cluster adsorption energy increases to 7.65 eV. Bader charge analysis shows that the $Au_{15}Cu_{15}$ cluster is strongly negatively charged (-3.54 e). In comparison with the defect-free case, the F-center has now donated its two additional electrons to the cluster. Similar behavior has been reported for other MgO-supported Au clusters, which are also negatively charged on F-centers.[9,10,17,52] The Au atom above the F-center is negatively charged by -1.27 e, which differs considerably from the defect-free case (-0.37 e). The rest of the Au atoms are negatively charged down to -0.5 e and all Cu atoms are positively charged up to +0.3 e. The charge transfer from the F-center has both local and nonlocal components as approximately one half of the charge transferred locates in the pointing Au atom and the rest is mainly distributed across the other Au atoms.

We have also considered another adsorption position with F-center in the middle of the cluster bottom plane (below Cu atom). The optimized adsorption geometry (C_s) is given in the Supporting Information [Figure S1(a-b)]. The configuration is 0.90 eV less stable than the F-center below an Au atom, and the net charge of the cluster is -3.36 e. The facing Cu atom above the F-center is strongly negatively charged with -0.83 e which is in a marked contrast compared to the defect-free surface (+0.27 e). The location of the defect has a deep influence on the charge transfer at the cluster-support interface.

For Mg-vacancy (V-center), the defect locates below the center of the bottom layer of $Au_{15}Cu_{15}$ cluster [Figure 1(g-h)]. The supported cluster retains the fcc pyramidal structure (C_{2v}) after optimization [Figure 1(g)]. The V-center adsorption causes that the bond lengths of Au-O and Cu-O decrease down to 2.57-2.92 Å and 1.91-1.94 Å, respectively. The binding energy of $Au_{15}Cu_{15}$/MgO is the highest (9.40 eV) for all supports. Despite the inherent electron-depletion in the vacancy, the cluster still receives electron density from the support. However, the charge transfer is the smallest in this case (Table 1) although the interaction between the support and cluster is the strongest. There are two reasons for the reduced charge transfer on the V-center. First, Mg atoms donate electrons in

ionic bonding (MgO), and in the case of a missing Mg atom, the substrate makes less charge donation to the cluster. Second, the four Cu atoms around the V-center lose more electrons (~0.3 e, each) than those on the defect-free surface (~0.19 e, each). From above, we can see that there is no direct relationship between the interaction energy and the charge transfer for AuCu/MgO systems, and that the amount of charge transfer relates primarily to the supports with different defects (e.g. F-center).

To gain more insight on the electronic structure with different supports, a detailed analysis of the molecular orbitals has been performed through the examination of the projected density of states (PDOS), which includes the contribution of *s*, *p* and *d* orbital components. Figure 2 gives the PDOS of $Au_{15}Cu_{15}$/MgO(100) with F-center. The PDOS is projected on Au and Cu atoms within the cluster and Mg and O atoms on the surface layer of MgO. For the defect-free and V-center supports, the corresponding PDOS are given in Figure S2. For the highest occupied energy levels, the contributions of *p*- and *d*-orbitals of Au and Cu atoms (cluster) are the most prominent, while the *p*-orbitals of O atoms (support) also have visible weight.

In order to discern the difference in the PDOS, the *d*-band center has been calculated by

$$C_d = \frac{\int_{-\infty}^{\varepsilon_f} \rho \varepsilon d\varepsilon}{\int_{-\infty}^{\varepsilon_f} \rho d\varepsilon} \tag{7}$$

for the $Au_{15}Cu_{15}$ cluster on different supports. Here ε is the energy of each state, ρ is the corresponding density of *d*-states, and ε_f is the Fermi level. The C_d values are -2.91eV, -2.76eV, and -3.17eV, respectively, for $Au_{15}Cu_{15}$ on the defect-free, F-center, and V-center supports. The F-center support pushes the *d*-band center higher than the two others due to the strong charge (electron) transfer towards the cluster adsorbate.

To visualize the interaction between $Au_{15}Cu_{15}$ cluster and MgO support, Figure 3 gives the charge density differences (CDD) of the $Au_{15}Cu_{15}$/MgO(100) systems. CDD is calculated as:

$$\Delta\rho = \rho(Au_{15}Cu_{15} + MgO)) - \rho(Au_{15}Cu_{15}) - \rho(MgO) \tag{8}$$

where $\rho(X)$ is the electron density of system X. CDD shows the interaction at the interface between the AuCu cluster and MgO substrate, and it is especially pronounced (strong) for the vacancy regions of the F- and V-centers. In addition, the visualizations of the HOMO and LUMO states for the systems with different supports are displayed in Figure S3. Combined with the information in PDOS and CDD, one can see that the bonding between the MgO support and AuCu cluster is coupled to the hybridization of Au-5*d*, Cu-3*d*, and O-2*p* orbitals, in agreement what has been reported for an MgO supported Au cluster.[9]

On the whole, the binding between $Au_{15}Cu_{15}$ and MgO(100) increases from the defect-free surface to F-center, and then to V-center. The cluster is negatively charged on all three supports, and the F-center exhibits the strongest net charge transfer. All Au atoms gain electrons, while Cu atoms lose electrons except the ones above the F-center. This can be explained by differences in electron negativities, which are 2.4 and 1.9 for Au and Cu, respectively.[53] The average bond lengths (Table 1) show almost no change for the three cases. Together with the cluster symmetry changes from C_{2v} to C_s, and then back to C_{2v}, we can see that the structural fluctuation is very weak on different supports.

3.2. Reaction Mechanisms for CO Oxidation

The general consensus is that large dissociation energy barriers hinder the dissociation of O_2 on Au.[54,55] The bimolecular Langmuir-Hinshelwood (LH) mechanism has been commonly used to describe the reaction of Au clusters catalytic CO oxidation, which involves an OCOO* intermediate formation and the following breaking of the O-O bond.[4,5] However, recent experimental and computational studies have revealed that O_2 can adsorb dissociatively on Cu clusters.[46,56] Moreover, both the Eley-Rideal (ER) and LH pathways were considered for CO oxidation on Cu clusters.[46,57] We address here both reaction pathways using the most stable binding geometries of $Au_{15}Cu_{15}$/MgO(100) with or without defects.

3.2.1. Adsorption and Dissociation of O_2 Molecule

The optimal binding sites of O_2 molecule on the $Au_{15}Cu_{15}$ cluster with MgO(100) supports were located via extensive adsorption site sampling. The symmetrically inequivalent atop, edge, and face binding sites were systematically tested, including different molecular orientations. Similarly, the 2×O atoms were placed independently on different cluster surface binding sites representing dissociated configurations. A full geometry optimization was performed for all starting configurations. Here, the adsorption energy and the barrier height for dissociation are the two key parameters. For a given arrangement of O_2 or 2×O adsorption, the adsorption energy (E_{ad}^2) was computed as

$$E_{ad}^2 = E(Au_{15}Cu_{15}/MgO) + E(adsorbant) - E(Au_{15}Cu_{15}/MgO + adsorbant) \quad (9)$$

where *E(X)* is the total energy of system *X*. For the O_2 dissociative adsorption, *E(adsorbate)* corresponds to the total energy of the triplet state, the correct spin state of gas phase O_2. The O_2 dissociation processes and the energy barriers were calculated by the CI-NEB method.[45]

The geometries of the reactant, the transition state and the product of the identified lowest-energy reaction path for the O-O bond cleavage on the F-center surface are shown in Figure 4. For the defect-free and V-center supports, the corresponding reaction paths are given in Figure S4. The adsorption energies (E_{ad}^2) of O_2 and 2×O, bond length of O_2 (r_{O-O}), charge transfer (Q) to O_2 and 2×O, and activation energy barrier ($O_2 \rightarrow O + O$) for the most stable adsorption complex are listed in Table 2. The corresponding values for CO molecule adsorption are also included in Table 2.

The adsorption patterns of O_2 and 2×O are similar on $Au_{15}Cu_{15}$ with different MgO supports (Figures 4 and S4). Moreover, both O_2 and 2×O prefer binding sites on Cu atoms. For the O_2 molecule, the bridge site at the edge of $Au_{15}Cu_{15}$ is the preferable adsorption with the molecule parallel to a Cu–Cu bond. For dissociated O_2, the most stable configuration is the one where the two O atoms are located on the neighboring hollow sites. This route for O_2 adsorption (chemisorption) is energetically more favorable, and there is more charge transfer (Table 2).

The O_2 adsorption energy is lowest for the cluster on the F-center and highest on the V-center

support. A reverse sequence is found for the 2×O adsorption. The O_2 bond length is significantly expanded in all cases, having a maximum (1.41 Å) on the F-center. The calculated dissociative reaction barriers are very small on all supported clusters, but in particularly on the F-center (0.15 eV). From the above results, we can see that the F-center activates the dissociation of molecular O_2, and that this is due to additional charge from the support which is mediated by the AuCu cluster.

Activation energy barriers for O_2 dissociation have been reported on Cu clusters[46] and low index Cu surfaces.[58] The calculated energy barriers on Cu_{20} and Cu_{20}^- clusters were 0.51 eV and 0.14 eV, respectively.[46] On the low index Cu(100) and Cu(111) surfaces,[58] dissociation energies of 0.46-0.47 eV were observed. Furthermore, the two lowest energy dissociation channels on the Cu(110) surface corresponded to energy barriers of 0.15eV and 0.22 eV along the [100] and [$1\bar{1}0$] directions, respectively.

3.2.2. LH Mechanism

The LH reaction mechanism is initiated by the co-adsorption of CO and O_2 (with or without dissociation). We have screened the most stable co-adsorption configurations for CO + O_2, CO + 2×O, and CO + O on $Au_{15}Cu_{15}$/MgO(100) with different supports, and they are shown in Figure S5 (Supporting Information, see also Table S1). For CO + O_2, the preferable co-adsorption pattern involves the top site for CO and the bridge site for O_2 on $Au_{15}Cu_{15}$. However, the underlying metal atom site varies for CO depending on the support. For the defect-free surface, CO binds on an Au site near the AuCu/MgO(100) interface. For F-center, CO locates on the Cu atom at the face center of the pyramidal $Au_{15}Cu_{15}$ cluster. For V-center, CO adsorbs on an Au atom at the vertex of the cluster. While the O_2 bond length is significantly elongated, the C=O bond is hardly influenced upon adsorption.

The co-adsorption of CO + O_2 is the crucial initial step for CO oxidation according to previous studies.[4,54] Generally, it is argued that the molecule with a stronger adsorption energy is likely to cover the cluster first. Here, the adsorption energy of a single CO is 0.70-0.84 eV with the different

supports, which is higher than those for O_2 (Table 2). Furthermore, the co-adsorption energies are slightly higher than the sum of single O_2 and CO adsorption energies by 0.09-0.20 eV, which means that the co-adsorption systems are energetically lower than those of the individual adsorbates. A previous study of CO oxidation on Au clusters also found a relatively strong CO binding as compared to O_2, leading to CO poisoning and a low oxidation rate.[59]

The CO adsorption sites vary case-by-case on $Au_{15}Cu_{15}$ for the co-adsorption of CO + 2×O and CO + O depending on the MgO support. There is almost no charge transfer for CO adsorption on Au sites, while the Cu sites exhibit charge transfer of 0.10-0.25 e towards CO. The adsorbed O atoms are strongly negatively charged, similarly as in Table 2 for the pre-dissociation case.

The catalytic reaction pathways of CO oxidation are shown Figures 5 and 6 for the lowest energy co-adsorption sites with the defect-free and F-center MgO(100) supports (the same for the V-center is displayed in Figure S6). To compare the energies easily, the activation and reaction energies of different reaction pathways are summarized in Table 3.

Upon the co-adsorption of CO and O_2 on the defect-free surface (Figure 5), the molecules move closer to each other, followed by the breaking of O-O bond to form the first CO_2 molecule. The activation energy barrier is 0.93 eV, and the C=O bond is practically unchanged (1.16 Å) in the TS state. After the first CO_2 molecule release, the remaining oxygen atom is negatively charged by 0.97 e, and co-adsorption of a new CO molecule leads to formation of another CO_2 with a barrier of 0.66 eV (middle row in Figure 5). The resulting CO_2 is ejected out from the cluster. After this step, the catalytic cycle for CO* + O_2* is completed. Furthermore, the first CO_2 formation may involve an alternative reaction path, CO* + O* + O* ↔ O* + CO_2, and this is shown in the bottom row of Figure 5. The corresponding TS configuration has an activation energy of 0.74 eV. The rest of the catalytic cycle repeats the step with a single oxygen, CO* + O* ↔ CO_2.

For the F-center case (Figure 6), CO and O_2 move closer to each other to form the TS state with an elongated O-O bond of 1.43 Å (C=O bond is 1.17 Å). The formation of the first CO_2 molecule

involves a very small energy barrier (TS) of 0.16 eV, which is much less than that without the defect on MgO(100). For the dissociated O_2 (bottom row), the same energy barrier is 0.42 eV, while CO moves from a bridge to a top Cu site with no change in the bond length (1.17 Å) during the process. The second CO_2 formation involves a reaction barrier of 0.55 eV.

3.2.3. ER Mechanism

The ER mechanism involves an attack of a gaseous CO molecule on a pre-adsorbed O_2 or 2×O on $Au_{15}Cu_{15}$/MgO(100). The reaction pathways are displayed in Figure 7 for the F-center support and Figures S7 and S8 for the defect-free and V-center supports. The corresponding energy barriers are listed in Table 3. The reaction schemes on $Au_{15}Cu_{15}$/MgO(100) with and without defects are similar. The calculated activation energy barriers for CO + O_2* vary between 0.07-0.33 eV on the AuCu cluster at different MgO(100) surfaces. Apparently, the F-center support (lowest energy barrier) is the most favorable towards CO oxidation, which stems from the high-degree of activation of O_2 upon adsorption on $Au_{15}Cu_{15}$. However, it should be noted that the LH mechanism (and the corresponding TS) is lower in energy overall due to the adsorption energies of both CO and O_2 (or 2×O). Correspondingly, the ER reactions (Table 3) are systematically higher in the absolute energy scale due to the missing CO adsorption.

The subsequent step is CO oxidation with the remaining O atom. The corresponding reaction barriers (Table 3) are small again, and the pathways for a direct O abstraction by the gaseous CO molecule are displayed in Figures 7, S7 and S8. The abstraction of the second oxygen for 2×O repeats the pathway for CO+O*.

3.3. Microkinetic Model Analysis

To further investigate the catalytic activity of the $Au_{15}Cu_{15}$/MgO(100) system under different conditions, a 7-step microkinetic model was developed based on the DFT calculations. We emphasize that this model is a simplification compared to the molecular reactions studied here. The microkinetic model ignores the two O* containing (predissociated) pathways and the model does

not include atomistic details of the reactions. However, it allows us to address the real experimental variables, such as partial pressures and temperatures. It also includes the average surface coverage effects which were not addressed in the DFT calculations and complements these results.

Although no direct experimental data has been reported for CO oxidation on MgO-supported AuCu clusters, CO oxidation on Au/MgO has been studied extensively.[9,17] Especially, Yoon[9] *et al.* found that CO_2 was produced at 140 K and 280 K on F-center-rich Au_8/MgO(100) thin films. On the contrary, almost no CO_2 was obtained on defect-free MgO(100) thin films. Inspired by this, we have used temperatures at 150 K and 300 K in combination with different partial pressures [$P(CO)$ = 1×10^{-4} bar – 1 bar, $P(O_2)$ = 5×10^{-1} bar – 2 bar] in the microkinetic model to evaluate catalyst coverages and CO_2 formation at longer time scales. The elementary steps and the details of the model are described in the Supporting Information and the results are collected in Table 4.

Table 4 shows that the CO_2 formation rate on the F-center support with $P(CO)$ = 1×10^{-2} bar and $P(O_2)$ = 5×10^{-1} bar is much higher than that on the other two supports, while the defect-free and V-center supports are comparable with each other. Moreover, the rate of CO_2 formation increases with temperature. Interestingly, at higher CO partial pressures (1 bar or 5×10^{-1} bar), the coverage of CO is high, while that of molecular and atomic oxygen remains negligible for all three MgO supports. The DFT calculation showed us above that CO binding is stronger than O_2, and this leads to CO poisoning of the cluster surface. This indicates that a high CO partial pressure hinders the oxidation process because of the lack of oxygen source. Tuning the CO partial pressure smaller (1×10^{-2} bar or 1×10^{-4} bar) affects the CO coverage considerably, especially on the F-center support. Moreover, the rate of CO_2 formation is already high at 150 K on the F-center support. For the defect- free and V-center supports, the rate of CO_2 formation increases noticeably as the CO/O_2 ratio is decreased [$P(CO)$ = 1×10^{-4} bar, $P(O_2)$ = 2.0 bar] and the temperature is increased to 300 K. Based on these observations, we chose to investigate further the conditions at which the CO_2 formation rate appears relatively high.

Figure 8(a) shows the coverages of reactant species (O_2, CO, O) and the turn-over frequency (TOF) of CO_2 from microkinetic model simulations as a function of time for the F-center support at low temperature [T = 150 K, $P(CO)$ = 1×10^{-2} bar, $P(O_2)$ = 5×10^{-1} bar]. Throughout the process, the coverage of O remains at a high level, while the coverage of O_2 is negligible. The CO overage is saturated at a moderate level. Moreover, CO_2 production stays constant after the steady state is reached. This combination of coverages is beneficial for CO_2 formation. Previously, the DFT calculations showed that O_2 dissociates easily to O atoms on the AuCu cluster. From Figure 8(a), we conclude that O_2 molecules dissociate immediately after adsorption or they are rapidly consumed in the CO oxidation processes (LH mechanism), which keep the coverage of O_2 molecules negligible.

Figure 8(b) shows the effect of varying O_2 pressures on the rate of CO_2 formation at long time scales with different CO partial pressures at T = 150 K. For similar partial pressures of O_2 and CO there is no CO_2 production due to the CO poisoning of the cluster surface. Correspondingly, we chose to tune the CO partial pressures between 1×10^{-3} bar and 1×10^{-1} bar. For $P(CO)$ = 1×10^{-1} bar, there is no CO_2 production in this range of O_2 pressures. As the pressure is decreased to $P(CO)$ = 5×10^{-2} bar, we can see the onset of the CO_2 formation at the oxygen partial pressure of 2.8 bar. A further decrease down to $P(CO)$ = 1×10^{-2} bar results in that the CO_2 formation starts already at low O_2 partial pressures and it saturates rapidly at a high level [$P(O_2)$ = 1.5-3.5 bar]. Even smaller partial pressure $P(CO)$ = 5×10^{-3} bar shifts the threshold and saturation points of CO_2 formation at lower oxygen partial pressures and reduces the formation rate. The same trend continues for $P(CO)$ = 1×10^{-3} bar.

For the defect-free and the V-center supports, $P(CO)$ = 1×10^{-4} bar, $P(O_2)$ = 2 bar, and T = 300 K were chosen to analyze the coverages of species (O_2, CO, O) and TOF of CO_2 in Figure 9. For the defect-free case [Figure 9(a)], the O_2 coverage decreases from 0.5 below 0.1, while the CO coverage increases close to 0.9. The coverage of O (dissociated oxygen) remains negligible.

Obviously, CO is blocking O_2 which causes that the TOF of CO_2 does not reach high levels.

For the V-center support [Figure 9(b)], the coverage of O rapidly reaches a high level at the expense of the molecular oxygen. The CO coverage remains negligible throughout the process. The high coverage of O atoms is beneficial here since the reaction barriers are considerably lower than for the direct attack on the adsorbed O_2 (Table 3). While the trends are rather different between the two cases in Figure 9, the value in the TOF of CO_2 is not significantly pronounced for the V-center support. On the whole, the F-center support is most active for CO_2 formation, and the observed rates differ drastically with respect to the latter two cases.

The microkinetic modeling above considers rather high O_2 partial pressures, and this may cause copper oxidation in a longer time scale. We note that our DFT calculations focus on low O_2 and CO concentrations and we have not studied the effect of several oxygen molecules (or oxidation). However, the dissociation barriers of O_2 (as presented in Table 2) are higher than those of the CO + O* + O* → CO_2 +O* reaction (in Table 3). Therefore, O_2 dissociation is slower in this reaction channel than CO_2 formation and the oxide formation is unlikely based on these arguments.

4. SUMMARY

We have investigated the atomic CO oxidation mechanisms on the MgO-supported $Au_{15}Cu_{15}$ cluster by combining DFT simulations with microkinetic modeling. We have systemically considered the cluster on the defect-free, F-center (O-vacancy), and V-center (Mg-vacancy) MgO(100) supports. Our calculations reveal that the supports induce negative charge transfer to the $Au_{15}Cu_{15}$ cluster, and that the effect is pronounced for the F-center (3.54 e). In all cases, the adsorption energy of CO is stronger than that of O_2 and the stability of the co-adsorption (CO + O_2) system is higher than the sum of the individual adsorbates. The CO adsorption sites vary between Cu and Au sites, while the oxygen species prefer Cu.

O_2 can be effectively activated upon adsorption and dissociated to 2×O atoms by crossing low energy barriers of 0.15-0.24 eV. The LH reaction barriers for CO_2 production are significantly reduced on the F-center (0.16 eV). The ER reaction barriers are lower than those of LH mechanism for all three supports, but this mechanism is not favorable due to missing CO absorption (energy, entropic contributions). The microkinetic modeling based on the collected DFT results confirms that $Au_{15}Cu_{15}$ on the F-center support is the most beneficial for CO_2 production as it can catalyze CO oxidation already at the low-temperature (150 K), as long as the CO partial pressure is kept low (the optimal combination is $P(CO) = 1\times10^{-2}$ and $P(O_2) = 2$ bar). The catalyst surface is highly sensitive to CO and gets poisoned when the partial pressure is increased. Selecting the right partial pressures for CO and O_2 turns out to be important for high CO_2 production. Furthermore, the MgO(100) support itself can be tuned more active by introducing defects, for example, via sputtering.

Finally, we want to mention that conflicting experimental results have been reported for the catalytic activity of AuCu catalysts towards CO oxidation. Especially, the effect of redox treatments on AuCu nanoparticles is still debated.[60-62] In practice, several factors influence the catalytic performance of bimetallic nanoparticles, *e.g.*, nanostructure, composition, size, and the chemical structure of the support (including the defects). Our theoretical results show that AuCu clusters are potential catalyst for CO oxidation, although different substrates may result in subtle changes in the Au and Cu sites, and this causes that the catalytic process is a complex problem.

ASSOCIATED CONTENT

Supporting Information

The Supporting Information is available.

Details of the microkinetic model; Properties of the most stable co-adsorption configurations (Table S1); $Au_{15}Cu_{15}$/MgO(100) with the O-vacancy below the Cu atom (Figure S1); PDOS of the

$Au_{15}Cu_{15}$ on the defect-free and V-center supports (Figure S2); HOMO and LUMO orbitals (Figure S3); O_2 dissociation on $Au_{15}Cu_{15}$/MgO(100) with the defect-free and V-center surfaces (Figure S4); The most stable co-adsorption configurations (Figure S5); CO oxidation on $Au_{15}Cu_{15}$/MgO(100) with the V-center surface by LH mechanism (Figure S6); CO oxidation on $Au_{15}Cu_{15}$/MgO(100) with the defect-free and V-center surfaces by ER mechanism (Figure S7 and S8).

AUTHOR INFORMATION

Corresponding Author

*E-mail: jaakko.akola@tut.fi. Phone: +358 40 198 1179.

ACKNOWLEDGEMENTS

The DFT calculations were carried out in CSC - the IT Center for Science Ltd., Espoo, Finland. Financial support has been provided by the Academy of Finland through its Centre of Excellence Program (Project 284621).

REFERENCES

(1) Haruta, M.; Kobayashi, T.; Sano, H.; Yamada, N. Novel Gold Catalysts for the Oxidation of Carbon Monoxide at a Temperature Far Below 0 ˚C. *Chem. Lett.* **1987**, 16, 405-408.

(2) Grabow, L. C.; Mavrikakis, M. Nanocatalysis Beyond the Gold-Rush Era. *Angew. Chem. Int. Edit.* **2008**, 47, 7390-7392.

(3) Hutchings, G J.; Brust, M.; Schmidbaur, H. Gold - an Introductory Perspective. *Chem. Soc. Rev.* **2008**, 37, 1759-1765.

(4) Gao, Y.; Shao, N.; Pei, Y.; Chen, Z.; Zeng, X. Catalytic Activities of Subnanometer Gold Clusters (Au_{16}-Au_{18}, Au_{20}, and Au_{27}-Au_{35}) for CO oxidation. *ACS nano.* **2011**, 5, 7818-7829.

(5) Li, L.; Gao, Y.; Li, H.; Zhao, Y.; Pei, Y.; Chen, Z.; Zeng, X. CO Oxidation on TiO_2 (110) Supported Subnanometer Gold Clusters: Size and Shape Effects. *J. Am. Chem. Soc.* **2013**, 135, 19336-19346.

(6) Herzing, A. A.; Kiely, C. J.; Carley, A. F.; Landon, P.; Hutchings, G. J. Identification of Active Gold Nanoclusters on Iron Oxide Supports for CO Oxidation. *Science.* **2008**, 321, 1331-1335.

(7) Chen, M. S.; Goodman, D. W. The Structure of Catalytically Active Gold on Titania. *Science* **2004**, 306, 252-255.

(8) Sanchez, A.; Abbet, S.; Heiz, U.; Schneider, W. D.; Häkkinen, H.; Barnett, R. W.; Landman, U. When Gold is Not Noble: Nanoscale Gold Catalysts. *J. Phys. Chem. A.* **1999**, 103, 9573-9578.

(9) Yoon, B.; Häkkinen, H.; Landman, U.; Wörz, A. S.; Antonietti, J. M.; Abbet, S.; Judai, K.; Heiz, U. Charging Effects on Bonding and Catalyzed Oxidation of CO on Au_8 Clusters on MgO. *Science* **2005**, 307, 403-407.

(10) Nikbin, N.; Austin N.; Vlachos, D. G.; Stamatakis, M.; Mpourmpakis, G. Catalysis at the Sub-nanoscale: Complex CO Oxidation Chemistry on a Few Au Atoms. *Catal. Sci. Technol.* **2015**, 5, 134-141.

(11) Iizuka, Y.; Fujiki, H.; Yamauchi N.; Chijiiwaa, T.; Arai, S.; Tsubotab, S.; Haruta, M. Adsorption of CO on Gold Supported on TiO_2. *Catal. Today* **1997**, 36, 115-123.

(12) Boccuzzi, F.; Chiorino, A.; Manzoli, M.; Andreeva, D.; Tabakova, T. FTIR Study of the Low-Temperature Water-Gas Shift Reaction on Au/Fe_2O_3 and Au/TiO_2 Catalysts. *J. Catal.* **1999**, 188, 176-185.

(13) Schubert, M. M.; Hackenberg, S.; van Veen, A C.; Muhler, M.; Plzak, V.; Behm, R. J. CO Oxidation over Supported Gold Catalysts - "Inert" and "Active" Support Materials and Their Role for the Oxygen Supply During Reaction. *J. Catal.* **2001**, 197, 113-122.

(14) Comotti, M.; Li, W. C.; Spliethoff, B.; Schuth, F. Support Effect in High Activity Gold Catalysts for CO Oxidation. *J. Am. Chem. Soc.* **2006**, 128, 917-924.

(15) Meyer, R.; Lemire, C.; Shaikhutdinov, S. K.; Freund, H. Surface Chemistry of Catalysis by Gold. *Gold Bull.* **2004**, 37, 72-124.

(16) Remediakis, I. N.; Lopez, N.; Nørskov, J. K. CO Oxidation on Rutile-Supported Au Nanoparticles. *Angew. Chem.* **2005**, 117, 1858-1860.

(17) Stamatakis, M.; Christiansen, M A.; Vlachos, D G.; Mpourmpakis, G. Multiscale Modeling Reveals Poisoning Mechanisms of MgO-Supported Au Clusters in CO Oxidation. *Nano lett.* **2012**, 12, 3621-3626.

(18) Kobayashi, Y.; Nasu, S.; Tsubota, S.; Haruta, M. ^{197}Au Mössbauer Study of Nano-Sized Gold Catalysts Supported on $Mg(OH)_2$ and TiO_2. *Hyperfine Interact.* **2000**, 126, 95-99.

(19) Guzman, J.; Gates, B. C. Structure and Reactivity of a Mononuclear Gold-Complex Catalyst Supported on Magnesium Oxide. *Angew. Chem. Int. Edit.* **2003**, 42, 690-693.

(20) Guzman, J.; Gates, B. C. Catalysis by Supported Gold: Correlation between Catalytic Activity for CO Oxidation and Oxidation States of Gold. *J. Am. Chem. Soc.* **2004**, 126, 2672-2673.

(21) Guzman, J.; Carrettin, S.; Corma, A. Spectroscopic Evidence for the Supply of Reactive Oxygen during CO Oxidation Catalyzed by Gold Supported on Nanocrystalline CeO2. *J. Am. Chem. Soc.* **2005**, 127, 3286-3287.

(22) Boyd, D.; Golunski, S.; Hearne, G. R.; Magadzu, T.; Mallick, K.; Raphulu, M. C.; Venugopal, A.; Scurrell, M. S. Reductive Routes to Stabilized Nanogold and Relation to Catalysis by Supported Gold. *Appl. Catal. A: Gen.* **2005**, 292, 76-81.

(23) Hutchings, G J.; Hall, M S.; Carley, A. F.; Landon, P.; Solsona, B. E.; Kiely, C. J.; Herzing, A.; Makkee, M.; Moulijn, J. A.; Overweg, A.; et al. Role of Gold Cations in the Oxidation of Carbon Monoxide Catalyzed by Iron Oxide-Supported Gold. *J. Catal.* **2006**, 242, 71-81.

(24) Chen, M.; Goodman, D. W. Catalytically Active Gold: from Nanoparticles to Ultrathin Films. *Acc. Chem. Res.* **2006**, 39, 739-746.

(25) Lopez, N.; Janssens, T. V. W.; Clausen, B. S.; Xu, Y.; Mavrikakis, M.; Bligaard, T.; Norskov, J. K. On the Origin of the Catalytic Activity of Gold Nanoparticles for Low-Temperature CO Oxidation. *J. Catal.* **2004**, 223, 232-235.

(26) Bracey, C. L.; Ellis, P. R.; Hutchings, G. J. Application of Copper-Gold Alloys in Catalysis: Current Status and Future Perspectives. *Chem. Soc. Rev.* **2009**, 38, 2231-2243.

(27) Pauwels, B.; Van Tendeloo, G.; Zhurkin, E.; Hou, M.; Verschoren, G.; Theil Kuhn, L.; Bouwen, W.; Lievens, P. Transmission Electron Microscopy and Monte Carlo Simulations of Ordering in Au-Cu Clusters Produced in a Laser Vaporization Source. *Phys. Rev. B.* **2001**, 63, 165406.

(28) Cerbelaud, M.; Barcaro, G.; Fortunelli, A.; Ferrando R. Theoretical Study of AuCu Nanoalloys Adsorbed on MgO (001). *Surf. Sci.* **2012**, 606, 938-944.

(29) Ferrando, R.; Jellinek, J.; Johnston, R. L. Nanoalloys: from Theory to Applications of Alloy Clusters and Nanoparticles. *Chem. Rev.* **2008**, 108, 845-910.

(30) Zhu, B.; Guo, Q.; Huang, X.; Wang, S.; Zhang, S.; Wu, S.; Huang, W. Characterization and Catalytic Performance of TiO_2 Nanotubes-Supported Gold and Copper Particles. *J. Mol. Catal. A: Chem.* **2006**, 249, 211-217.

(31) Yuan, Y.; Kozlova, A. P.; Asakura, K.; Wan, H.; Tsai, K.; Iwasawa, Y. Supported Au Catalysts Prepared from Au Phosphine Complexes and As-Precipitated Metal Hydroxides: Characterization and Low-Temperature CO Oxidation. *J. Catal.* **1997**, 170, 191-199.

(32) Smolentseva, E.; Bogdanchikova, N.; Simakov, A.; Pestryakov, A.; Tusovskaya, I.; Avalos, M.; Farías, M. H.; Díaz, J. A.; Gurin, V. Influence of Copper Modifying Additive on State of Gold in Zeolites. *Surf. Sci.* **2006**, 600, 4256-4259.

(33) Kameoka, S.; Tsai, A. P. CO Oxidation over a Fine Porous Gold Catalyst Fabricated by Selective Leaching from an Ordered $AuCu_3$ Intermetallic Compound. *Catal. Lett.* **2008**, 121, 337-341.

(34) Della Pina, C.; Falletta, E.; Rossi, M. Highly Selective Oxidation of Benzyl Alcohol to Benzaldehyde Catalyzed by Bimetallic Gold-Copper Catalyst. *J. Catal.* **2008**, 260, 384-386.

(35) Vaughan, O. P. H.; Kyriakou, G.; Macleod, N.; Tikhov, M.; Lambert, R. M. Copper as a Selective Catalyst for the Epoxidation of Propene. *J. Catal.* **2005**, 236, 401-404.

(36) Chimentao, R J.; Medina, F.; Fierro, J. L. G.; Llorca, J.; Sueiras, J. E.; Cesteros, Y.; Salagre, P. Propene Epoxidation by Nitrous Oxide over Au-Cu/TiO_2 Alloy Catalysts. *J. Mol. Catal. A: Chem.* **2007**, 274, 159-168.

(37) Llorca, J.; Dominguez, M.; Ledesma, C.; Chimentao, R. J.; Medina, F.; Sueiras, J.; Angurell, I.; Seco, M.; Rossell, O. Propene Epoxidation over TiO_2-supported Au-Cu Alloy Catalysts Prepared from Thiol-Capped Nanoparticles. *J. Catal.* **2008**, 258, 187-198.

(38) Perdew, J. P.; Burke, K.; Ernzerhof, M. Generalized Gradient Approximation Made Simple. *Phys. Rev. Lett.* **1996**, 77, 3865.

(39) VandeVondele, J.; Krack, M.; Mohamed, F.; Parrinello, M.; Chassaing, T; Hutter, J. Fast and Accurate Density Functional Calculations Using a Mixed Gaussian and Plane Waves Approach. *Comput. Phys. Commun.* **2005**, 167, 103-128.

(40) CP2K version 2.5. CP2K is freely available from http://www.cp2k.org.

(41) VandeVondele, J.; Hutter, J. Gaussian Basis Sets for Accurate Calculations on Molecular Systems in Gas and Condensed Phases. *J. Chem. Phys.* **2007**, 127, 114105.

(42) Goedecker, S.; Teter, M.; Hutter, J. Separable Dual-Space Gaussian Pseudopotentials. *Phys. Rev. B.* **1996**, 54, 1703.

(43) Xu, L.; Henkelman, G. Calculations of Ca Adsorption on a MgO(100) Surface: Determination of the Binding Sites and Growth Mode. *Phys. Rev. B.* **2008**, 77, 205404.

(44) Yu, M.; Trinkle, D. R. Accurate and Efficient Algorithm for Bader Charge Integration. *J. Chem. Phys.* **2011**, 134, 064111.

(45) Henkelman, G.; Uberuaga, B. P.; Jónsson, H. A Climbing Image Nudged Elastic Band Method for Finding Saddle Points and Minimum Energy Paths. *J. Chem Phys.* **2000**, 113, 9901-9904.

(46) Ma, L.; Melander, M.; Laasonen, K.; Akola, J. CO Oxidation Catalyzed by Neutral and Anionic Cu_{20} Clusters: Relationship between Charge and Activity. *Phys. Chem. Chem. Phys.* **2015**, 17, 7067-7076.

(47) Ma, L.; Melander, M.; Weckman, T.; Lipasti, S.; Laasonen, K.; Akola, J. DFT Simulations and Microkinetic Modelling of 1-Pentyne Hydrogenation on Cu_{20} Model Catalysts. *J. Mol. Graph. Model.* **2016**, 65, 61-70.

(48) Atkins, P.; De Paula, J. *Physical Chemistry*; Oxford University Press: Oxford, 2010.

(49) Gottfried J. M.; Schmidt, K. J.; Schroeder, S. L. M.; Christmann, K. Adsorption of Carbon Monoxide on Au(110)-1×2). *Surf. Sci.* **2003**, 536, 206-224.

(50) Kim, J.; Samano, E.; Koel, B. E. CO Adsorption and Reaction on Clean and Oxygen-Covered Au(211) Surfaces. *J. Phys. Chem. B* **2006**, 110, 17512-17517.

(51) Okada, M.; Moritani, K.; Goto, S.; Kasai, T.; Yoshigoe, A.; and Teraoka, Y. Actively Controlled Oxidation of Cu{100} with Hyperthermal O_2 Molecular Beam. *J. Chem. Phys.* **2003**, 119, 6994-6997.

(52) Coquet, R.; Hutchings, G. J.; Taylor, S. H.; Willock, D. J. Calculations on the Adsorption of Au to MgO Surfaces Using SIESTA. *J. Mater. Chem.* **2006**, 16, 1978-1988.

(53) Lide, D. R., *CRC Handbook of Chemistry and Physics, 84th Edition*; CRC Press: Florida, 2003.

(54) Liu. Z. P.; Hu, P.; Alavi, A. Catalytic Role of Gold in Gold-Based Catalysts: A Density Functional Theory Study on the CO Oxidation on Gold. *J. Am. Chem. Soc.* **2002**, 124, 14770-14779.

(55) Nikbin, N.; Mpourmpakis, G.; Vlachos, D. G. A Combined DFT and Statistical Mechanics Study for the CO Oxidation on the Au_{10}^{-1} Cluster. *J. Phys. Chem. C.* **2011**, 115, 20192-20200.

(56) Hirabayashi, S.; Ichihashi, M.; Kawazoe, Y.; Kondow, T. Comparison of Adsorption Probabilities of O_2 and CO on Copper Cluster Cations and Anions. *J. Phys. Chem. A.***2012**, 116, 8799-8806.

(57) Wang, Y.; Wu, G.; Yang, M.; Wang, J. Competition between Eley-Rideal and Langmuir-Hinshelwood Pathways of CO Oxidation on Cu_n and Cu_nO (n = 6, 7) Clusters. *J. Phys. Chem. C* **2013**, 117, 8767-8773.

(58) Diao, Z Y.; Han, L. L.; Wang, Z. X.; Dong, C. The Adsorption and Dissociation of O_2 on Cu Low-Index Surfaces. *J. Phys. Chem. B* **2005**, 109, 5739-5745.

(59) Kim, H. Y.; Lee, H. M.; Henkelman, G. CO Oxidation Mechanism on CeO_2-supported Au Nanoparticles. *J. Am. Chem. Soc.* **2012**, 134, 1560-1570.

(60) Liu, X.; Wang, A.; Li, L.; Zhang, T.; Mou, C. Y.; Lee, J. F. Structural Changes of Au-Cu Bimetallic Catalysts in CO Oxidation: in situ XRD, EPR, XANES, and FT-IR Characterizations. *J. Catal.* **2011**, 278, 288−296.

(61) Najafishirtari, S.; Brescia, R.; Guardia, P.; Marras, S.; Manna, L.; Colombo, M. Nanoscale Transformations of Alumina-Supported AuCu Ordered Phase Nanocrystals and Their Activity in CO Oxidation. *ACS Catal.* **2015**, 5, 2154-2163.

(62) Yin, J.; Shan, S.; Yang, L.; Mott, D.; Malis, O.; Petkov, V.; Cai, F.; Shan, N. M.; Luo, J.; Chen, B. H.; et al. Gold–Copper Nanoparticles: Nanostructural Evolution and Bifunctional Catalytic Sites. *Chem. Mater.* **2012**, 24, 4662−4674.

Table 1 Adsorption energy (E_{ad}^{1}), net charge (Q), bond length of Cu-O (r_{Cu-O}) and Au-O (r_{Au-O}), average bond length <R>, and symmetry of the $Au_{15}Cu_{15}$ cluster on three MgO supports.

$Au_{15}Cu_{15}$/MgO(100)	E_{ad}^{1} (eV)	Q (e)	r_{Cu-O} (Å)	r_{Au-O} (Å)	$< R >$ (Å)	symmetry
defect-free	5.42	-1.96	2.07-2.09	2.66-3.10	2.66	C_{2v}
F-center	7.65	-3.54	2.16-2.25	2.68-3.12	2.65	C_s
V-center	9.40	-0.87	1.91-1.94	2.57-2.92	2.66	C_{2v}

Table 2 Adsorption energy (E_{ad}^{2}) of O_2, 2×O and CO, bond length of O_2 (r_{O-O}) and CO ($r_{C=O}$) molecules, charge transfer (Q) from the adsorbent [$Au_{15}Cu_{15}$/MgO(100)] to the adsorbate (O_2, 2×O or CO), and activation energy barrier ($O_2 \rightarrow O + O$) for the lowest energy adsorption systems.

$Au_{15}Cu_{15}$/MgO(100)	E_{ad}^{2} (eV)			r_{O-O} (Å)	$r_{C=O}$ (Å)	Q (e)			Reaction (eV)
	O_2	2×O	CO	O_2	CO	O_2	2×O	CO	$O_2 \rightarrow O + O$
defect-free	0.51	1.96	0.75	1.35	1.15	0.69	1.82	0.05	0.23
F-center	0.40	2.00	0.84	1.41	1.15	0.84	1.83	0.08	0.15
V-center	0.52	1.74	0.70	1.34	1.15	0.68	1.82	0.03	0.24

Table 3 Calculated activation energy barriers (E_f) and the reaction energies (ΔH) for CO oxidation on the $Au_{15}Cu_{15}$/MgO(100). The symbol '*' refers to the atom or molecule being adsorbed on the $Au_{15}Cu_{15}$ cluster. Note that the starting configurations of the LH (three upper ones) and ER reactions (three lower ones) are different which affects the overall energetics, where LH is systematically lower due to CO adsorption.

Reaction	defect-free		F-center		V-center	
	E_f (eV)	ΔH (eV)	E_f (eV)	ΔH (eV)	E_f (eV)	ΔH (eV)
$CO^* + O_2^* \leftrightarrow CO_2 + O^*$	0.93	-3.72	0.16	-3.73	0.77	-3.68
$CO^* + O^* \leftrightarrow CO_2$	0.66	-1.12	0.55	-0.79	0.71	-1.15
$CO^* + O^* + O^* \leftrightarrow CO_2 + O^*$	0.74	-2.15	0.42	-2.15	0.51	-2.25
$CO + O_2^* \leftrightarrow CO_2 + O^*$	0.33	-4.52	0.07	-4.49	0.28	-4.47
$CO + O^* \leftrightarrow CO_2$	0.20	-2.01	0.19	-1.97	0.37	-2.01
$CO + O^* + O^* \leftrightarrow CO_2 + O^*$	0.11	-3.34	0.05	-3.05	0.24	-3.20

Table 4 The calculated coverage of species (θ_{CO}, θ_{O_2}, θ_O) and the rate (s^{-1}) of CO_2 formation (r_{CO_2}) at long time scales with different CO/O_2 partial pressures and different temperatures.

P(CO) = 1 bar, P(O_2) = 2 bar			P(CO) = 5×10^{-1} bar, P(O_2) = 5×10^{-1} bar	
defect-free	150K	300K	150K	300K
θ_{CO}	1.00	9.99×10^{-1}	1.00	9.99×10^{-1}
θ_{O_2}	9.56×10^{-18}	5.12×10^{-9}	1.32×10^{-17}	5.12×10^{-9}
θ_O	4.08×10^{-22}	3.34×10^{-11}	5.62×10^{-22}	3.34×10^{-11}
r_{CO_2}	4.80×10^{-16}	1.80×10^{-1}	3.31×10^{-16}	9.07×10^{-2}
F-center	150K	300K	150K	300K
θ_{CO}	1.0	9.99×10^{-1}	1.00	9.99×10^{-1}
θ_{O_2}	2.39×10^{-26}	2.25×10^{-13}	2.38×10^{-26}	2.18×10^{-13}
θ_O	2.59×10^{-22}	2.41×10^{-11}	2.59×10^{-22}	2.41×10^{-11}
r_{CO_2}	6.62×10^{-16}	1.93×10^{-1}	3.31×10^{-16}	9.64×10^{-2}
V-center	150K	300K	150K	300K
θ_{CO}	9.99×10^{-1}	9.99×10^{-1}	1.00	9.99×10^{-1}
θ_{O_2}	1.42×10^{-15}	7.26×10^{-11}	2.79×10^{-14}	7.26×10^{-11}
θ_O	2.26×10^{-12}	2.36×10^{-9}	8.05×10^{-11}	2.36×10^{-9}
r_{CO_2}	4.27×10^{-12}	1.78×10^{-2}	6.24×10^{-11}	8.91×10^{-3}
P(CO) = 1×10^{-2} bar, P(O_2) = 5×10^{-1} bar			P(CO) = 1×10^{-4} bar, P(O_2) = 2 bar	
defect-free	150K	300K	150K	300K
θ_{CO}	9.10×10^{-1}	9.99×10^{-1}	8.82×10^{-5}	8.60×10^{-1}
θ_{O_2}	4.00×10^{-2}	1.17×10^{-5}	4.90×10^{-1}	6.00×10^{-2}
θ_O	1.75×10^{-6}	7.68×10^{-8}	2.12×10^{-5}	4.25×10^{-4}
r_{CO_2}	2.07×10^{-2}	4.16	2.51×10^{-3}	2.31×10^{2}
F-center	150K	300K	150K	300K
θ_{CO}	2.16×10^{-1}	6.65×10^{-3}	5.30×10^{-6}	1.67×10^{-7}
θ_{O_2}	7.08×10^{-5}	9.18×10^{-3}	9.22×10^{-5}	9.42×10^{-3}
θ_O	7.83×10^{-1}	9.75×10^{-1}	9.99×10^{-1}	9.81×10^{-1}
r_{CO_2}	2.00×10^{4}	7.79×10^{7}	2.55×10^{2}	7.84×10^{5}
V-center	150K	300K	150K	300K
θ_{CO}	2.14×10^{-1}	9.99×10^{-1}	5.55×10^{-5}	4.88×10^{-3}
θ_{O_2}	7.23×10^{-4}	1.81×10^{-7}	9.39×10^{-4}	2.87×10^{-2}
θ_O	7.83×10^{-1}	5.92×10^{-6}	9.98×10^{-1}	9.37×10^{-1}
r_{CO_2}	1.75×10^{-2}	4.45×10^{-1}	2.26×10^{-4}	7.05×10^{2}

Figure 1 Optimized $Au_{15}Cu_{15}$ cluster geometry adsorbed on the MgO(100) support and the corresponding MgO(100) surface with a dashed square denoting the cluster position: (a) top view, (b) angular view with one layer of support, (c) side view, and (d) surface layer of the defect-free structure, (e) side view and (f) surface layer of the F-center structure, and (g) side view and (h) surface layer of the V-center structure. Color key: yellow, Au; coral, Cu; green, Mg; and red, O.

Figure 2 Projected electronic density of states (PDOS) of the $Au_{15}Cu_{15}$ cluster on the F-center support and the zoom-in near the Fermi energy in each panel. The PDOS are projected onto the Au and Cu atoms in $Au_{15}Cu_{15}$ cluster, and Mg and O atoms on the surface layer of MgO(100). The Fermi energy is set at zero. Note the different vertical scale between the panels.

Figure 3 Charge density difference (CDD) of the $Au_{15}Cu_{15}$ cluster adsorbed on (a) the defect-free, (b) F-center, and (c) V-center MgO(100) supports. Blue and pink colors represent charge depletion and accumulation, respectively. The isosurface values are ± 0.002 e/a_0^3.

Figure 4 Structures of the initial state (IS), transition state (TS), and final state (FS) of the lowest identified pathways for $O_2 \rightarrow O + O$ on $Au_{15}Cu_{15}$/MgO(100) with the F-center surface and the energy changes with respect to the IS. The symbol '*' refers to the atom or molecule being adsorbed on the $Au_{15}Cu_{15}$ cluster.

Figure 5 Structures of the initial state (IS), transition state (TS), and final state (FS) for the catalytic CO oxidation on $Au_{15}Cu_{15}$/MgO(100) with the defect-free surface by Langmuir–Hinshelwood (LH) mechanism and the energy changes with respect to the IS. The symbol '*' refers to the atom or molecule being adsorbed on the $Au_{15}Cu_{15}$ cluster.

Figure 6 Structures of the initial state (IS), transition state (TS), and final state (FS) for the catalytic CO oxidation on $Au_{15}Cu_{15}$/MgO(100) with the F-center surface by Langmuir–Hinshelwood (LH)

mechanism and the energy changes with respect to the IS. The symbol '*' refers to the atom or molecule being adsorbed on the $Au_{15}Cu_{15}$ cluster.

Figure 7 Structures of the initial state (IS), transition state (TS), and final state (FS) for the catalytic CO oxidation on $Au_{15}Cu_{15}$/MgO(100) with the F-center surface by Eley–Rideal (ER) mechanism and the energy changes with respect to the IS. The symbol '*' refers to the atom or molecule being adsorbed on the $Au_{15}Cu_{15}$ cluster.

Figure 8 (a) Coverages of the species (O_2, CO, O) and TOF of CO_2 from microkinetic model simulations on the $Au_{15}Cu_{15}$/MgO(100) catalyst with F-center as a function of time [$P(CO)$ = 1×10^{-2} bar, $P(O_2)$ = 5×10^{-1} bar, T = 150 K]. (b) Rate of CO_2 formation at long time scales as a function of O_2 pressure at $P(CO)$ = 1×10^{-1} bar, 5×10^{-2} bar, 1×10^{-2} bar, 5×10^{-3} bar, 1×10^{-3} bar and T = 150 K.

Figure 9 Coverages of the species (O_2, CO, O) and TOF of CO_2 from microkinetic model simulations on the $Au_{15}Cu_{15}$/MgO(100) catalyst with (a) the defect-free support and (b) V-center support as a function of time [$P(CO)$ = 1×10^{-4} bar, $P(O_2)$ = 2.0 bar, T = 300 K].

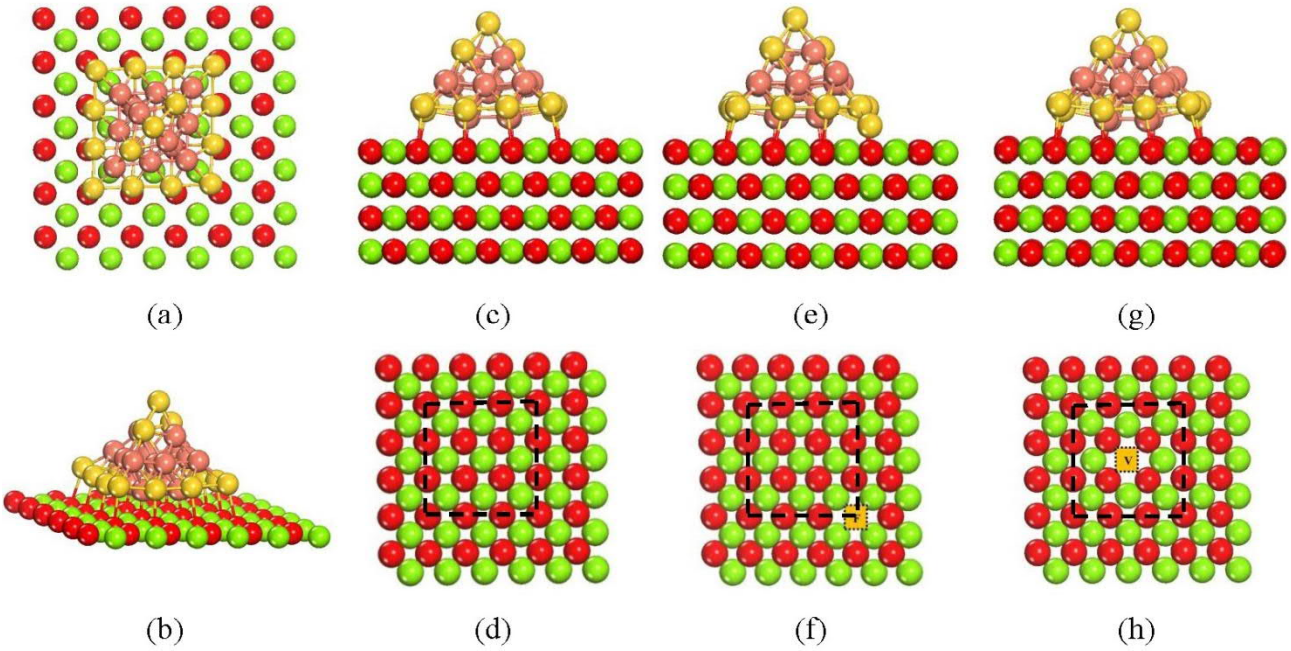

Figure 1

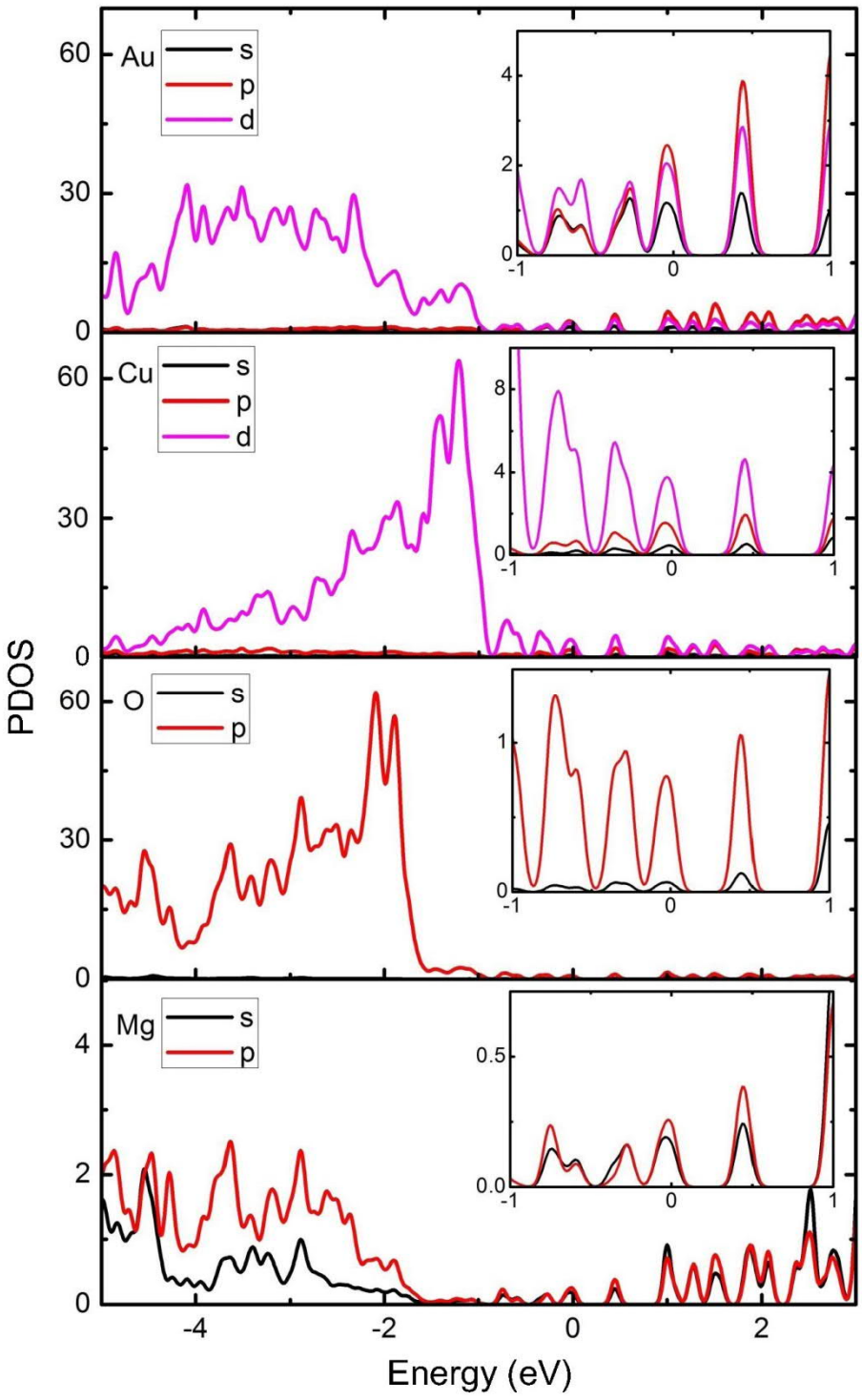

Figure 2

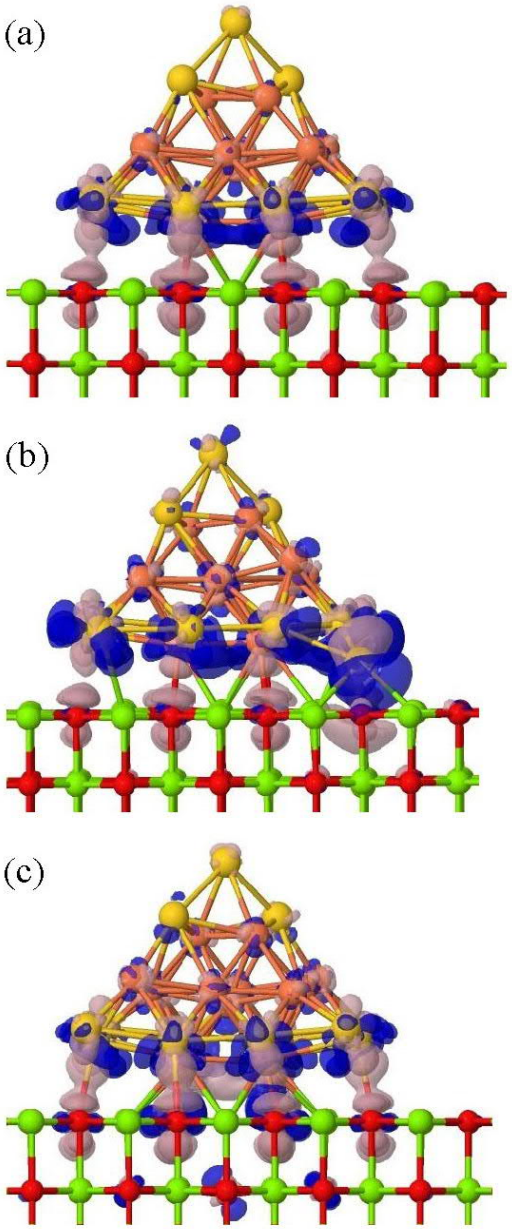

Figure 3

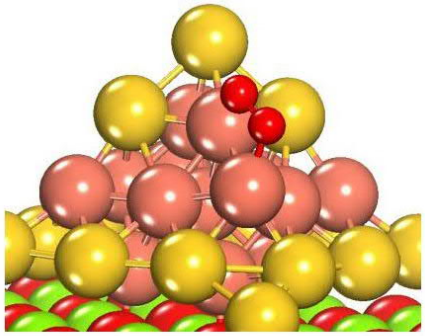

O_2*

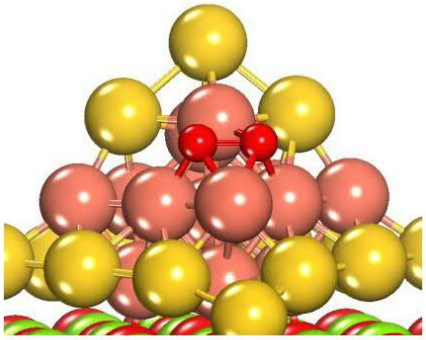

TS (0.15eV)

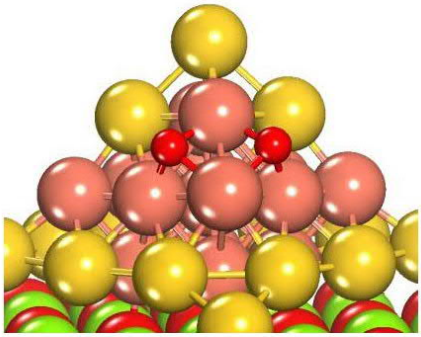

O* + O* (-1.60eV)

Figure 4

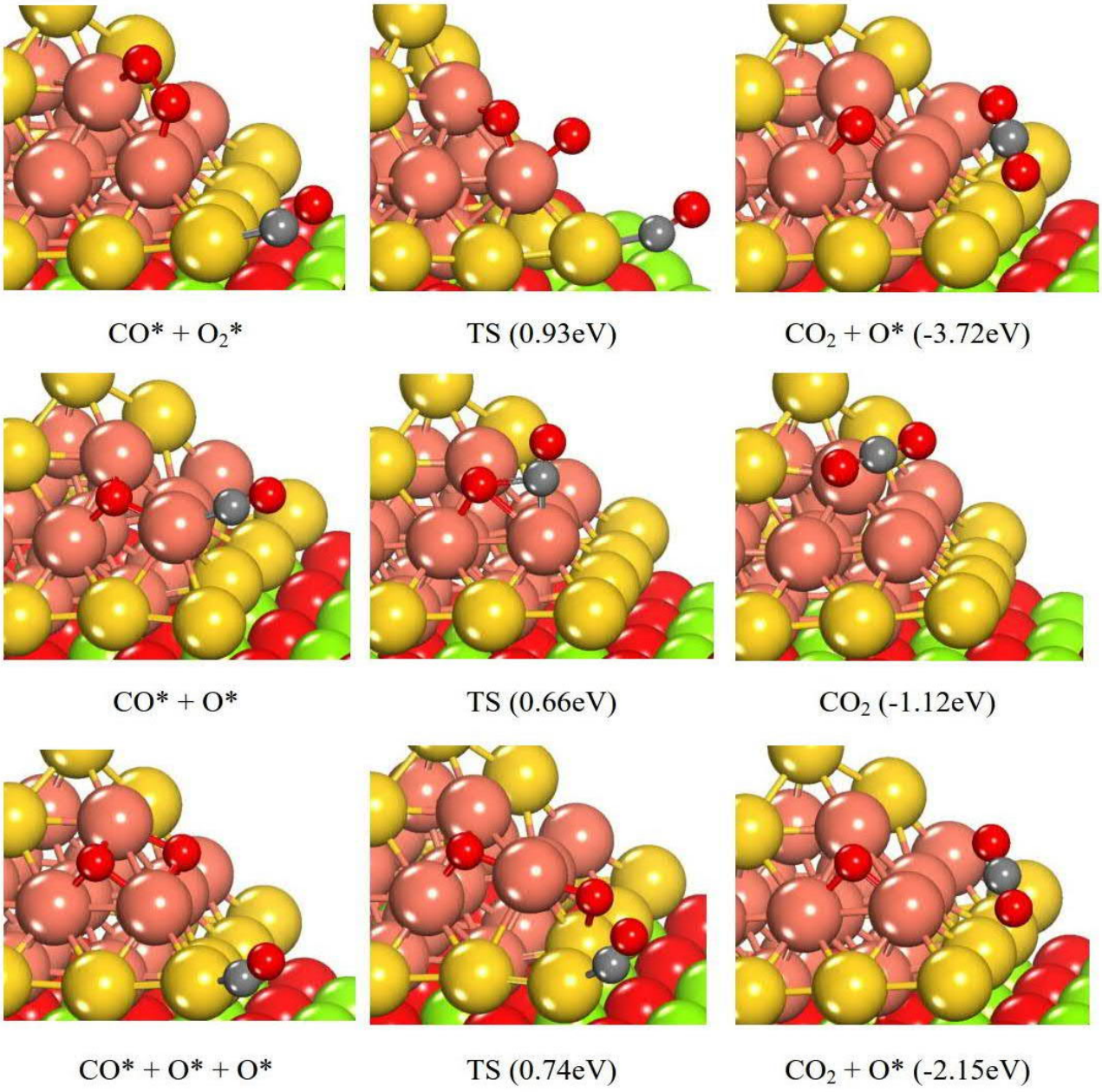
CO* + O2*
TS (0.93eV)
CO2 + O* (-3.72eV)
CO* + O*
TS (0.66eV)
CO2 (-1.12eV)
CO* + O* + O*
TS (0.74eV)
CO2 + O* (-2.15eV)

Figure 5

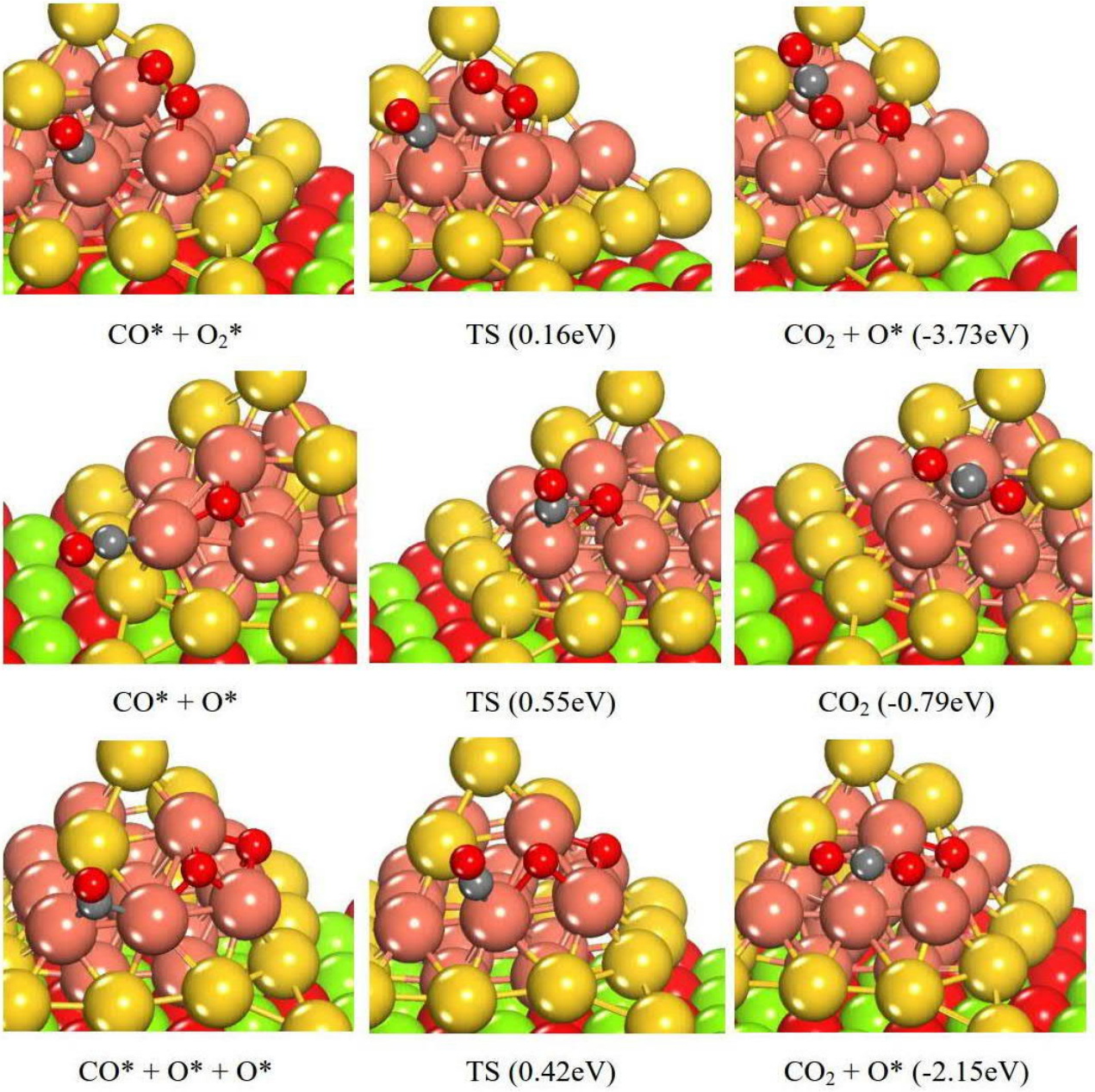
CO* + O2*
TS (0.16eV)
CO2 + O* (-3.73eV)
CO* + O*
TS (0.55eV)
CO2 (-0.79eV)
CO* + O* + O*
TS (0.42eV)
CO2 + O* (-2.15eV)

Figure 6

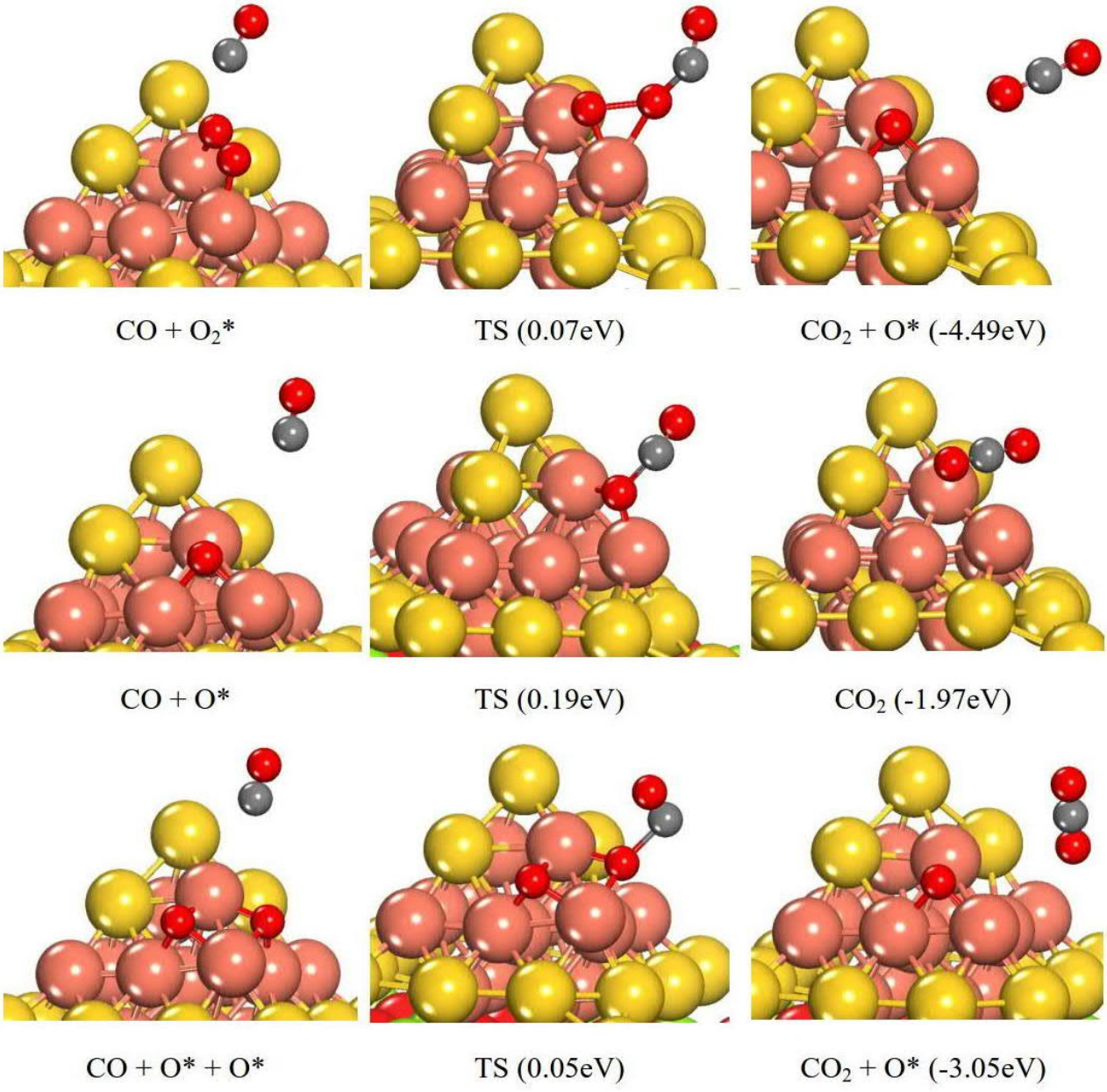
CO + O2*
TS (0.07eV)
CO2 + O* (-4.49eV)
CO + O*
TS (0.19eV)
CO2 (-1.97eV)
CO + O* + O*
TS (0.05eV)
CO2 + O* (-3.05eV)

Figure 7

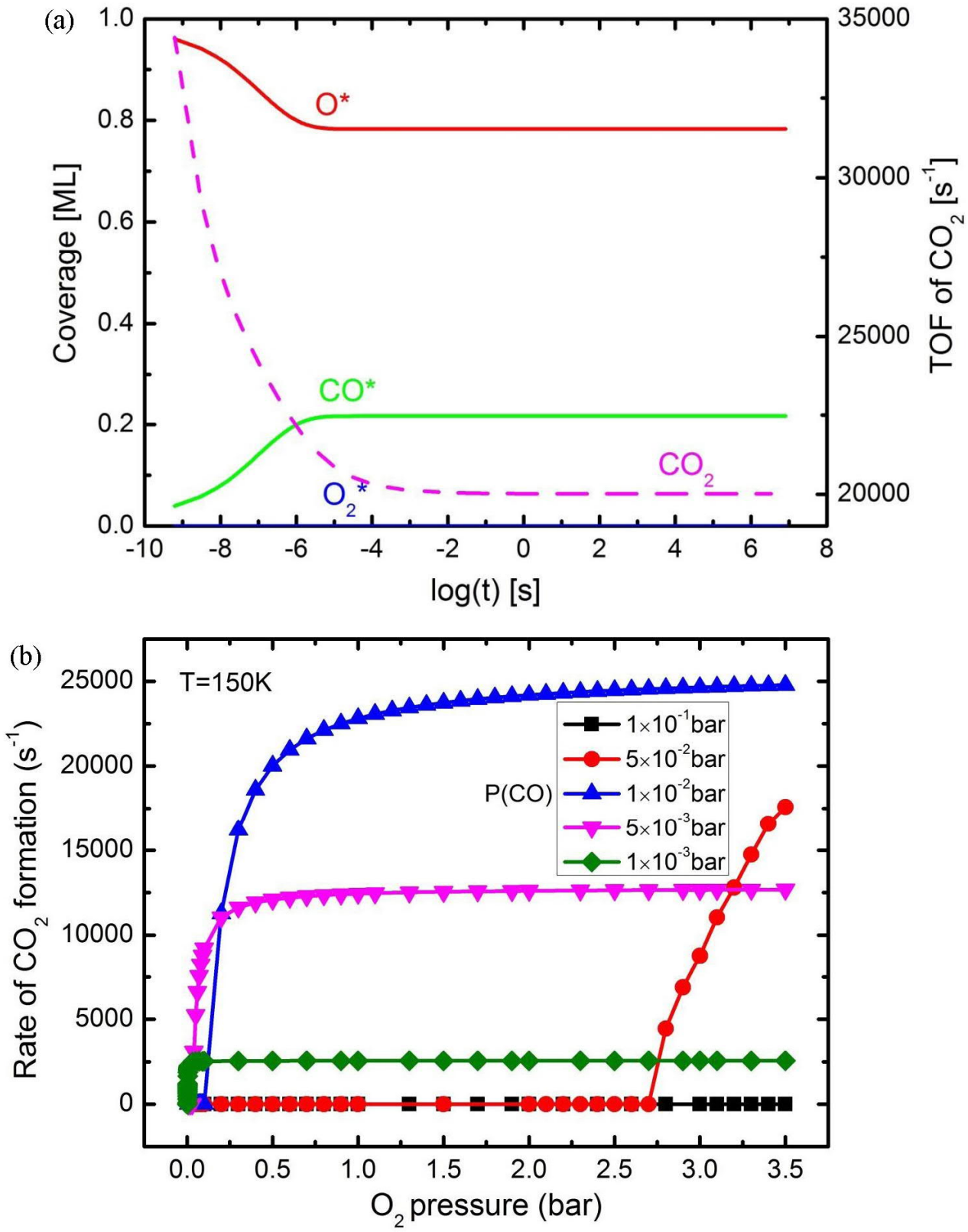
(a)
Coverage [ML]
TOF of CO2 [s-1]
log(t) [s]
O*
CO*
O2*
CO2
(b)
T=150K
Rate of CO2 formation (s-1)
O2 pressure (bar)
P(CO)
1×10-1bar
5×10-2bar
1×10-2bar
5×10-3bar
1×10-3bar

Figure 8

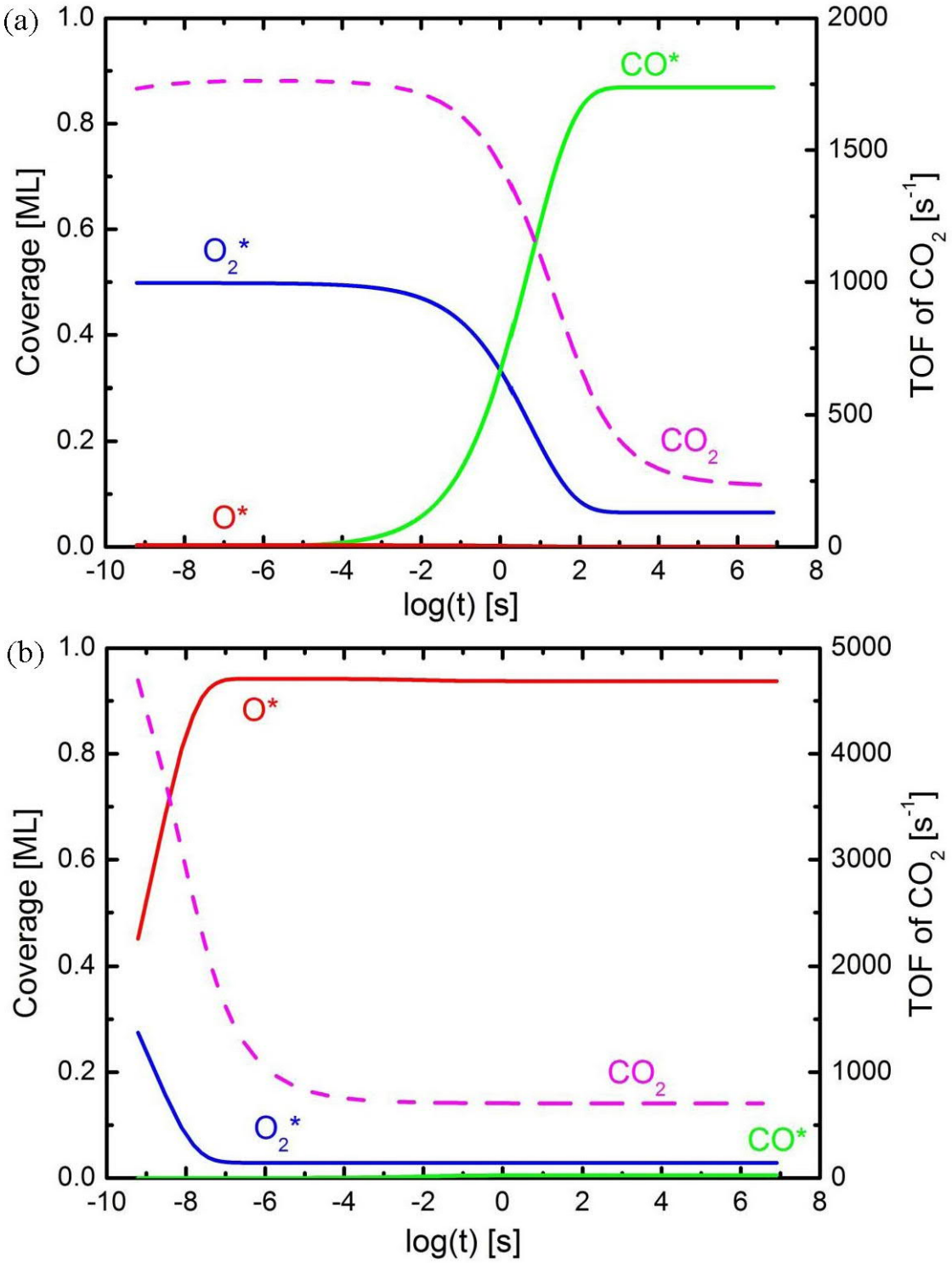
(a)
Coverage [ML]
TOF of CO2 [s-1]
log(t) [s]
CO*
O2*
CO2
O*
(b)
Coverage [ML]
TOF of CO2 [s-1]
log(t) [s]
O*
CO2
O2*
CO*

Figure 9

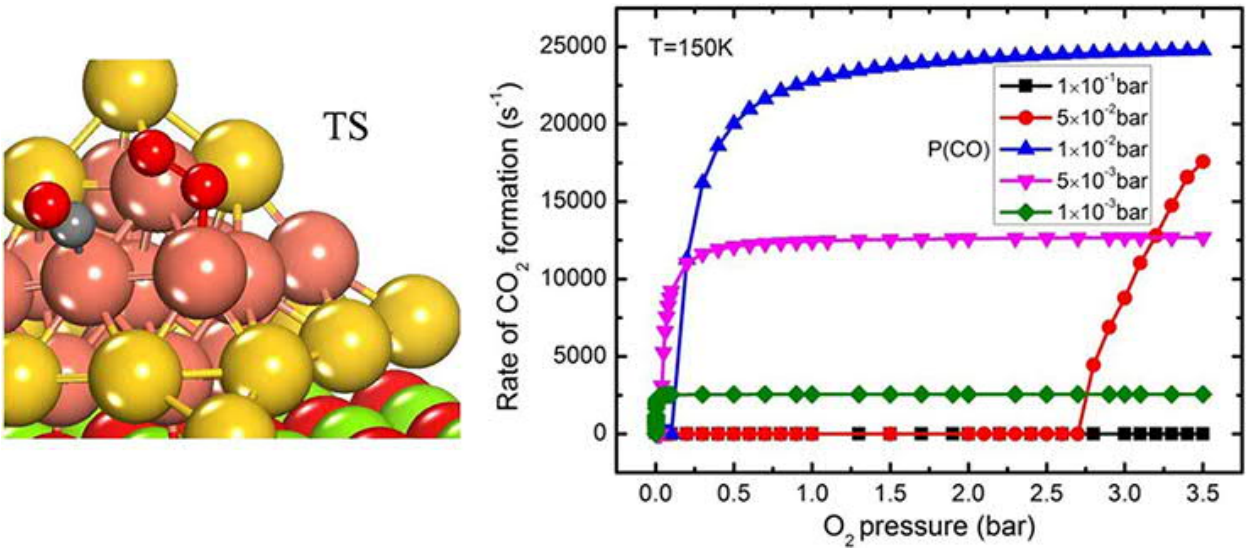

Table of Contents (TOC) Image

Supporting Information

CO Oxidation on the $Au_{15}Cu_{15}$ Cluster and the Role of Vacancies in the MgO(100) Support

Li Ma,[†,‡,§] Marko Melander,[§,¶] Timo Weckman,[§] Kari Laasonen,[§] and Jaakko Akola*[,†,‡]

[‡]Department of Physics, Tampere University of Technology, FI-33101 Tampere, Finland

[†]COMP Centre of Excellence, Department of Applied Physics, Aalto University, FI-00076 Aalto, Finland

[§]COMP Centre of Excellence, Department of Chemistry, Aalto University, FI-00076 Aalto, Finland

[¶]Department of Energy Conversion and Storage, Technical University of Denmark, DK-4000 Roskilde, Denmark

Corresponding Author

*E-mail: jaakko.akola@tut.fi. Phone: +358 40 198 1179.

Microkinetic Model

A microkinetic model was established to analyze the rates and selectivity in the O_2 dissociation and CO oxidation on $Au_{15}Cu_{15}$/MgO(100) with and without support vacancies. A 7-step reaction network was included as following:

$$O_2 + * \leftrightarrow O_2^* \quad (1)$$

$$CO + * \leftrightarrow CO^* \quad (2)$$

$$O_2^* + * \leftrightarrow 2O^* \quad (3)$$

$$CO^* + O_2^* \leftrightarrow CO_2 + O^* + * \quad (4)$$

$$CO^* + O^* \leftrightarrow CO_2 + 2* \quad (5)$$

$$CO + O_2^* \leftrightarrow CO_2 + O^* \quad (6)$$

$$CO + O^* \leftrightarrow CO_2 + * \quad (7)$$

An asterisk (*) represents a free site on the cluster surface. The reaction rates r_i were calculated using surface coverages θ_i, forward $k_{f,i}$ and backward $k_{r,i}$ rate constants:

$$r_1 = k_{f1}P(O_2)\theta_* - k_{r1}\theta_{O_2} \quad (8)$$

$$r_2 = k_{f2}P(CO)\theta_* - k_{r2}\theta_{CO} \quad (9)$$

$$r_3 = k_{f3}\theta_{O_2}\theta_* - k_{r3}\theta_O^2 \quad (10)$$

$$r_4 = k_{f4}\theta_{CO}\theta_{O_2} - k_{r4}P(CO_2)\theta_O\theta_* \quad (11)$$

$$r_5 = k_{f5}\theta_{CO}\theta_O - k_{r5}\,P(CO_2)\,\theta_*^2 \quad (12)$$

$$r_6 = k_{f6}P(CO)\theta_{O_2} - k_{r6}P(CO_2)\theta_O \quad (13)$$

$$r_7 = k_{f7}P(CO)\theta_O - k_{r7}P(CO_2)\theta_* \quad (14)$$

The θ_* is the coverage of unoccupied reaction sites on catalyst surface and *P(*)* is the partial pressure of a species. The rate constants were computed as shown in Eq.s 1-5 of the main paper.

Based on the reaction rates, the coverages of surface species and the production of CO_2 can be written with respect to time:

$$\frac{d}{dt}\theta_{O_2} = r_1 - r_3 - r_4 - r_6 \quad (15)$$

$$\frac{d}{dt}\theta_{CO} = r_2 - r_4 - r_5 \quad (16)$$

$$\frac{d}{dt}\theta_{O} = r_3 - r_5 + r_6 - r_7 \quad (17)$$

$$\frac{d}{dt}P_{CO_2} = r_4 + r_5 + r_6 + r_7 \quad (18)$$

The cumulative CO_2 production is written as

$$P_{CO_2} = \int_t dt \{r_4 + r_5 + r_6 + r_7\} \quad (19)$$

The surface coverages was constrained to fulfill

$$\sum_i \theta_i = 1 \quad (20)$$

From eq. 15-20, we can obtain surface coverages of different species and the production of CO_2 by simple integrations. In practice, the turn over frequency (TOF) value of CO_2 is more instructive,

$$TOF = \frac{P_{CO_2}}{t} \quad (21)$$

which can be obtained by eq. 21 at each time step.

Table S1 Adsorption energy of different adsorbates, bond length of the adsorbed O_2 and CO molecules (r_{O-O}, $r_{C=O}$), charge transfer (Q) from the adsorbent [$Au_{15}Cu_{15}$/MgO(100)] to the adsorbate (O or CO) for the adsorption systems in Figure S5.

Adsorbate	E_{ad}^2 (eV)	r_{O-O} (Å)	$r_{C=O}$ (Å)	Q (e)	
				O	CO
defect-free					
CO+O_2	1.35	1.36	1.16	0.71	0.04
CO+O+O	2.93		1.16	1.85	0.06
CO+O	2.43		1.16	1.00	0.13
O-vacancy					
CO+O_2	1.39	1.37	1.15	0.74	0.09
CO+O+O	2.93		1.17	1.86	0.23
CO+O	2.75		1.16	1.01	0.15
Mg-vacancy					
CO+O_2	1.42	1.34	1.16	0.66	0.02
CO+O+O	2.80		1.18	1.87	0.28
CO+O	2.42		1.16	1.00	0.12

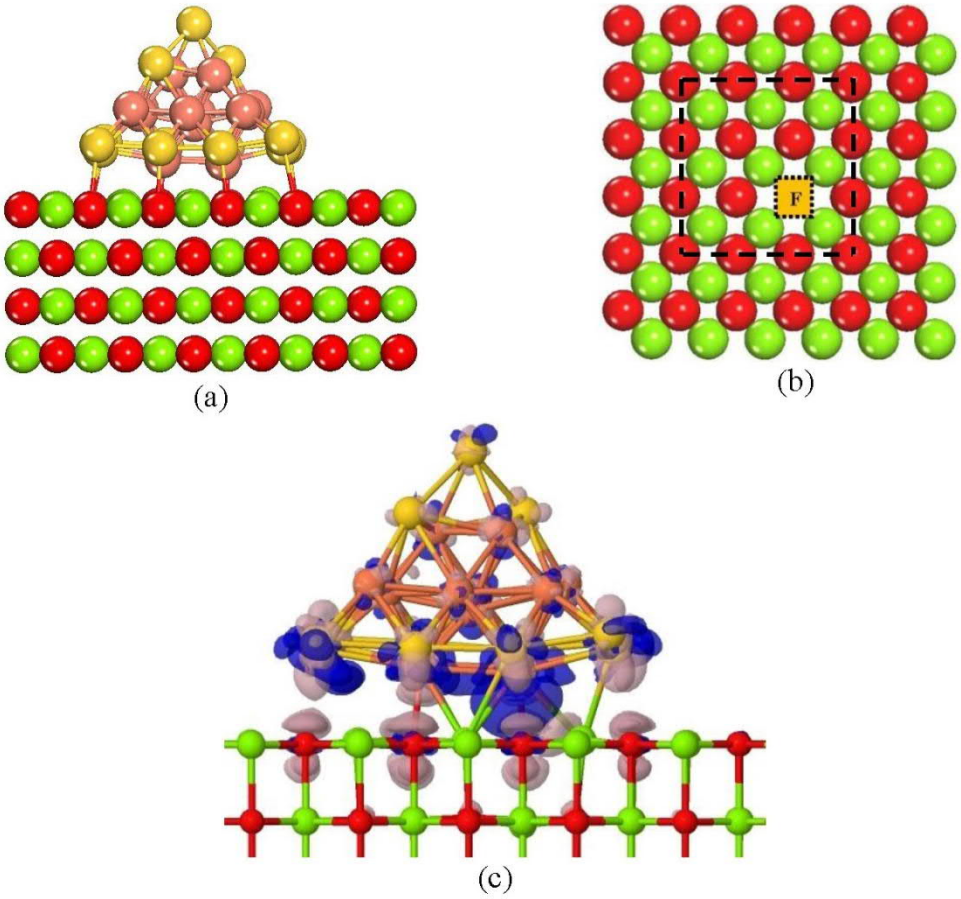

Figure S1 Optimized configures of (a) $Au_{15}Cu_{15}$ cluster adsorbed on an F-center MgO(100) with the O-vacancy below the Cu atom, (b) the corresponding MgO(100) surface with a dashed square denoting the cluster position, and (c) the charge density difference (CDD) of the corresponding system $Au_{15}Cu_{15}$/MgO(100) as in the main paper of Figure 3. Color key: yellow, Au; coral, Cu; green, Mg; and red, O.

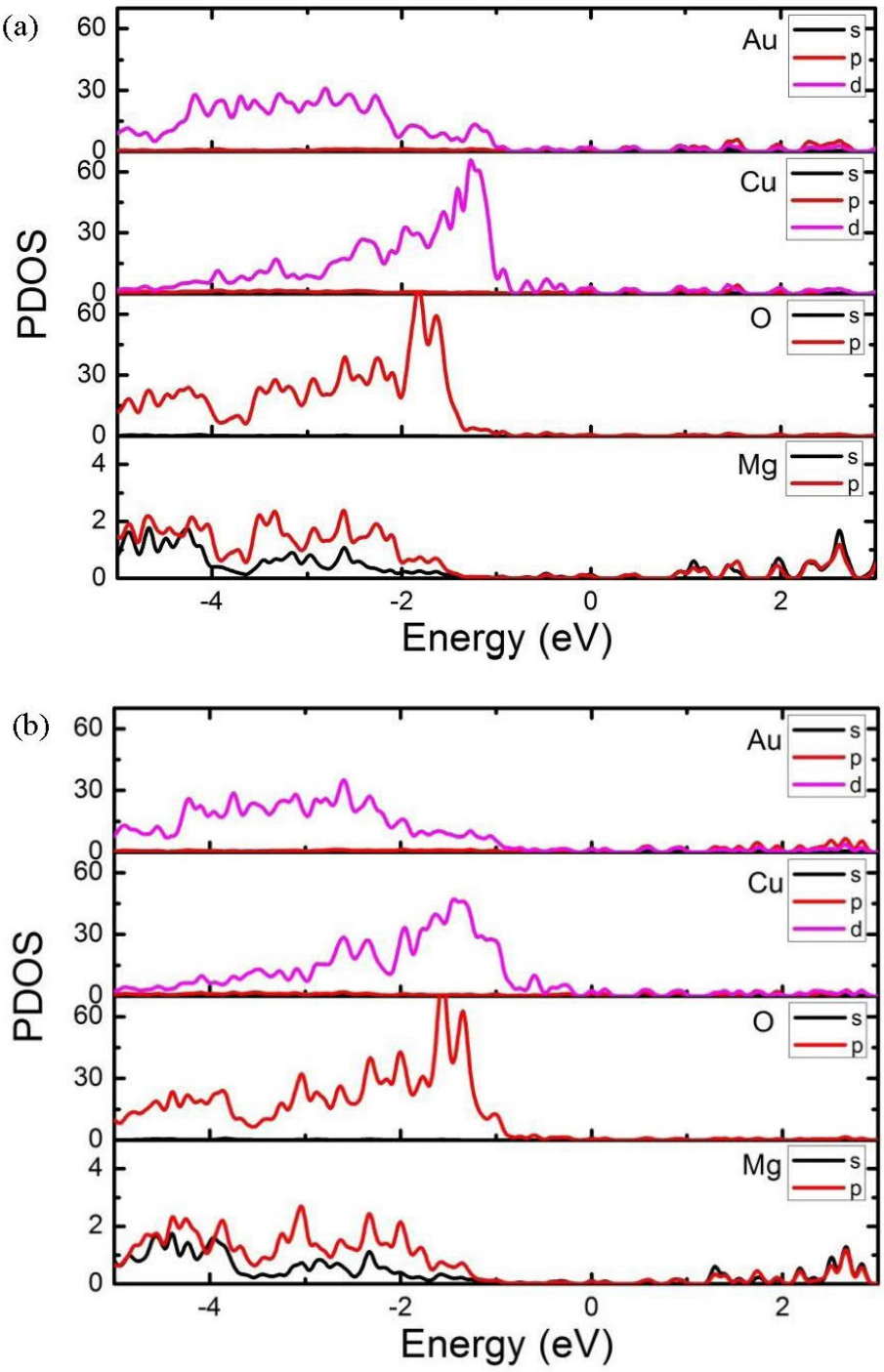

Figure S2 Projected electronic density of states (PDOS) of the $Au_{15}Cu_{15}$ cluster on (a) the defect-free and (b) V-center supports. The PDOS are projected onto the Au and Cu atoms in $Au_{15}Cu_{15}$ cluster, and Mg and O atoms on the surface layer of MgO(100). The Fermi energy is set at zero.

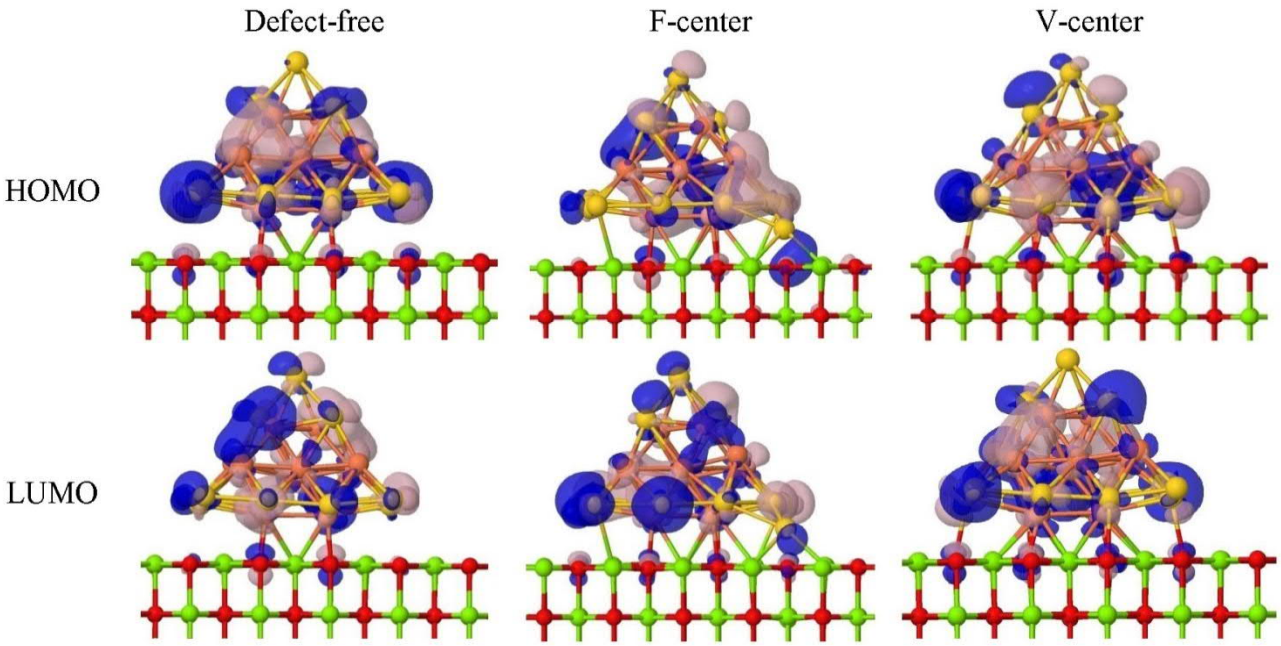

Figure S3 HOMO and LUMO orbitals of $Au_{15}Cu_{15}$ cluster adsorbed on the defect-free, F-center, and V-center MgO(100) surfaces. The isosurface values are 0.02 e/a_0^3.

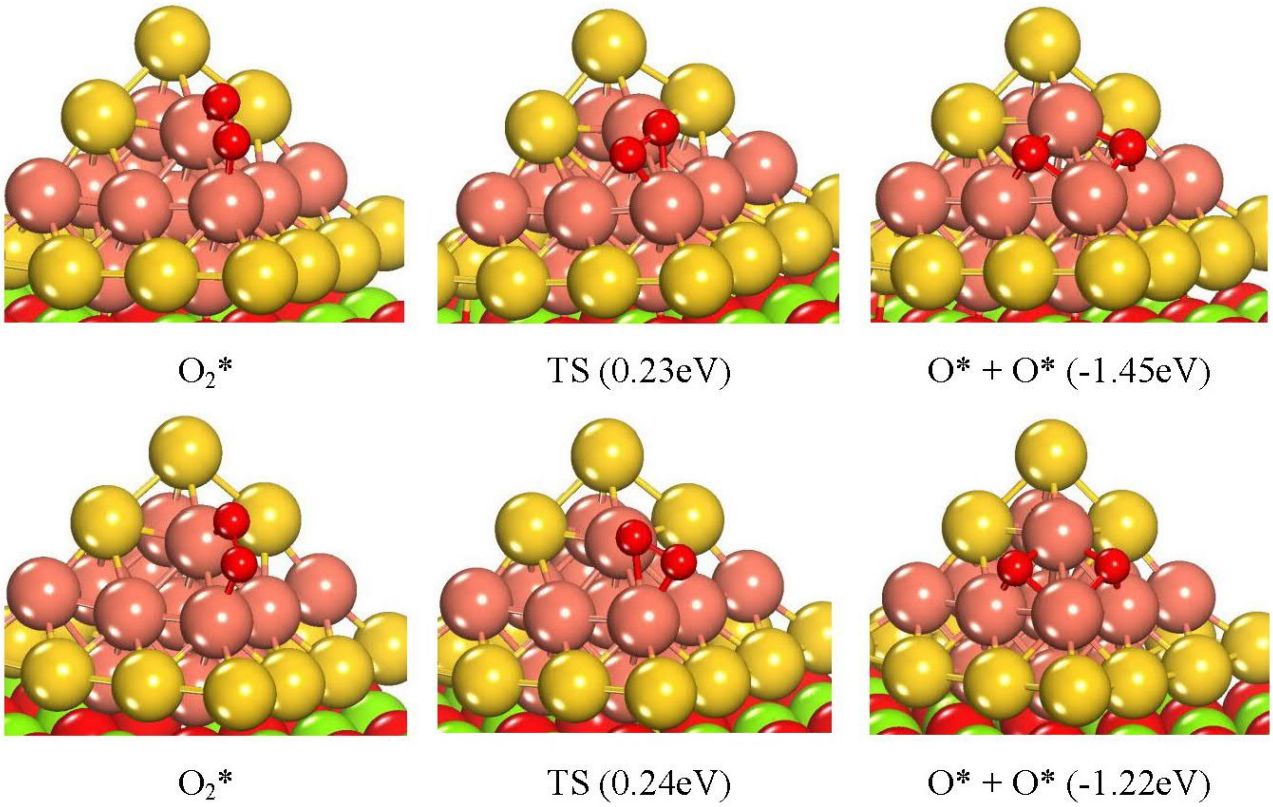

Figure S4 Structures of the initial state (IS), transition state (TS), and final state (FS) of the lowest identified pathways for $O_2 \rightarrow O + O$ on $Au_{15}Cu_{15}$/MgO(100) with the defect-free (first row) and V-center (second row) surfaces and the energy changes with respect to the IS. The symbol '*' refers to the atom or molecule being adsorbed on the $Au_{15}Cu_{15}$ cluster.

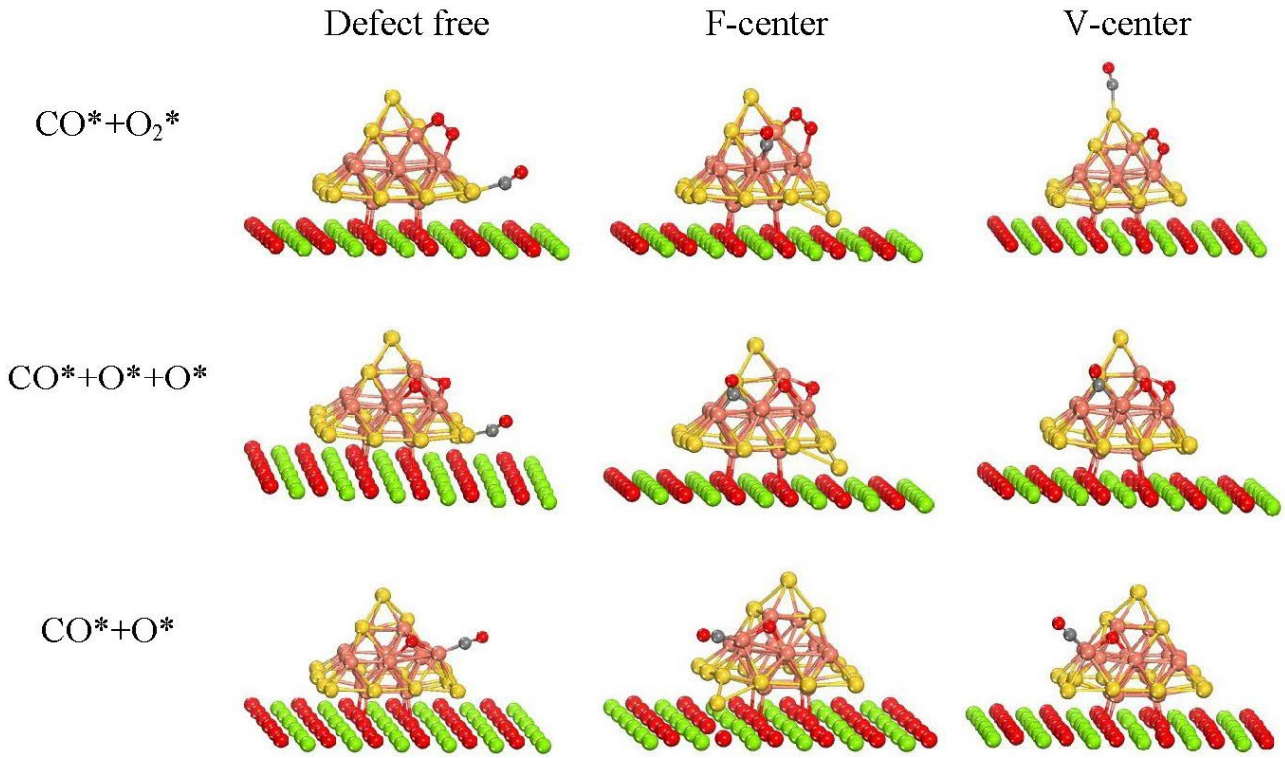

Figure S5. Most stable co-adsorption configurations of CO + O_2, CO + 2×O, and CO + O on $Au_{15}Cu_{15}$/MgO(100) with the defect-free, F-center, and V-center supports. Color key: yellow, Au; coral, Cu; green, Mg; red, O; and grey, C.

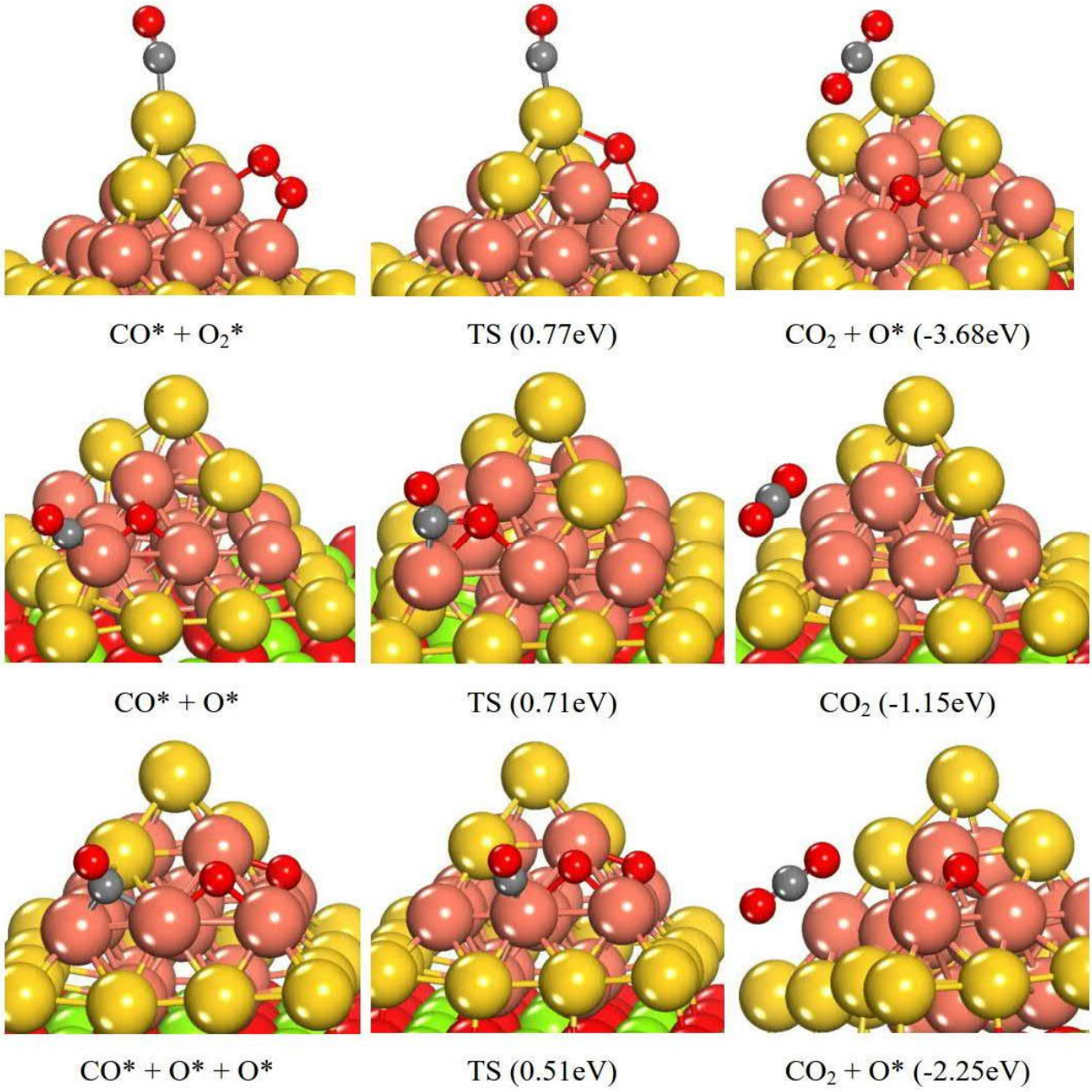

Figure S6 Structures of the initial state (IS), transition state (TS), and final state (FS) for the catalytic CO oxidation on $Au_{15}Cu_{15}$/MgO(100) with the V-center surface by Langmuir–Hinshelwood (LH) mechanism and the energy changes with respect to the IS. The symbol '*' refers to the atom or molecule being adsorbed on the $Au_{15}Cu_{15}$ cluster.

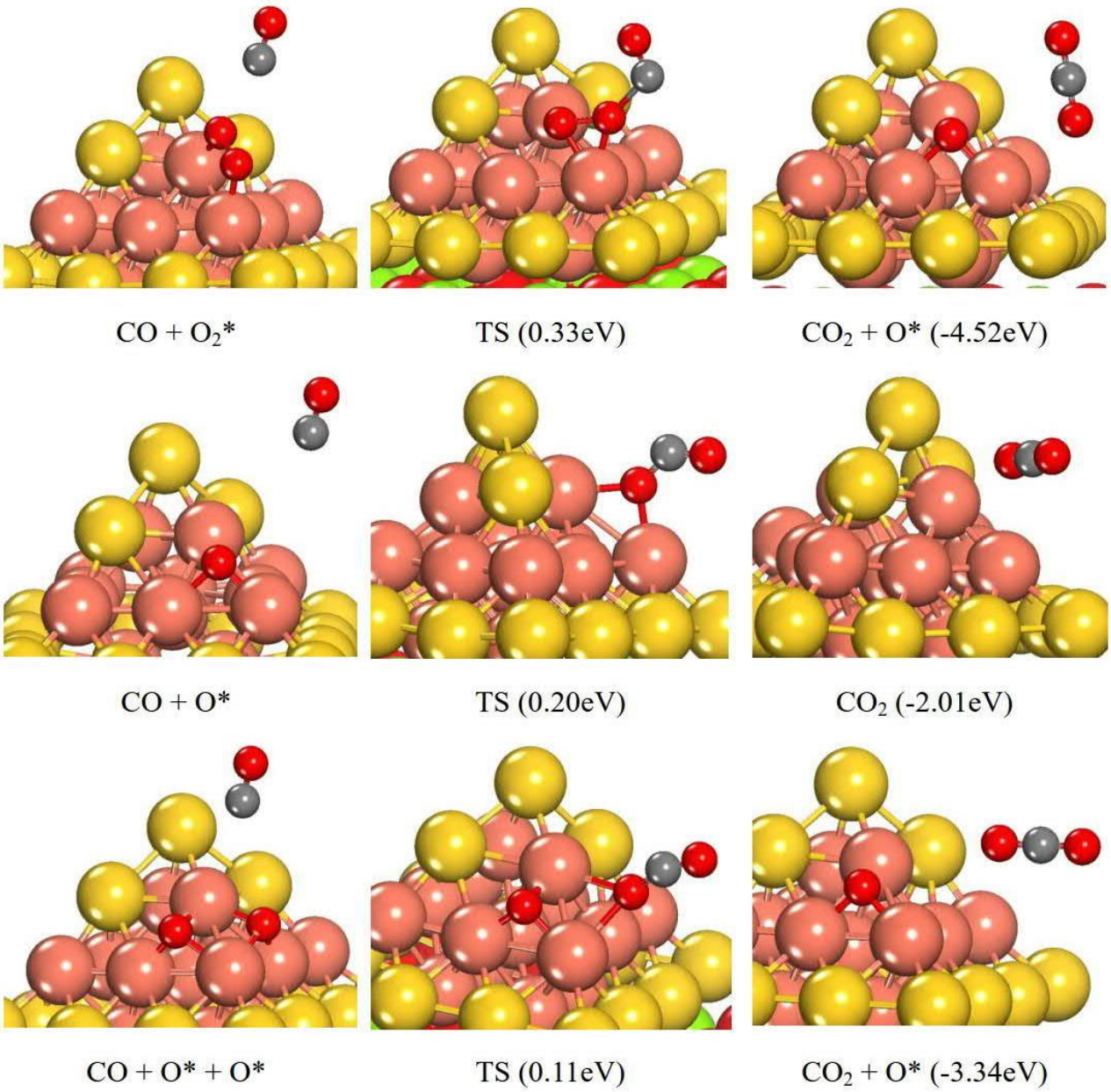

Figure S7 Structures of the initial state (IS), transition state (TS), and final state (FS) for the catalytic CO oxidation on $Au_{15}Cu_{15}$/MgO(100) with the defect-free surface by Eley–Rideal (ER) mechanism and the energy changes with respect to the IS. The symbol '*' refers to the atom or molecule being adsorbed on the $Au_{15}Cu_{15}$ cluster.

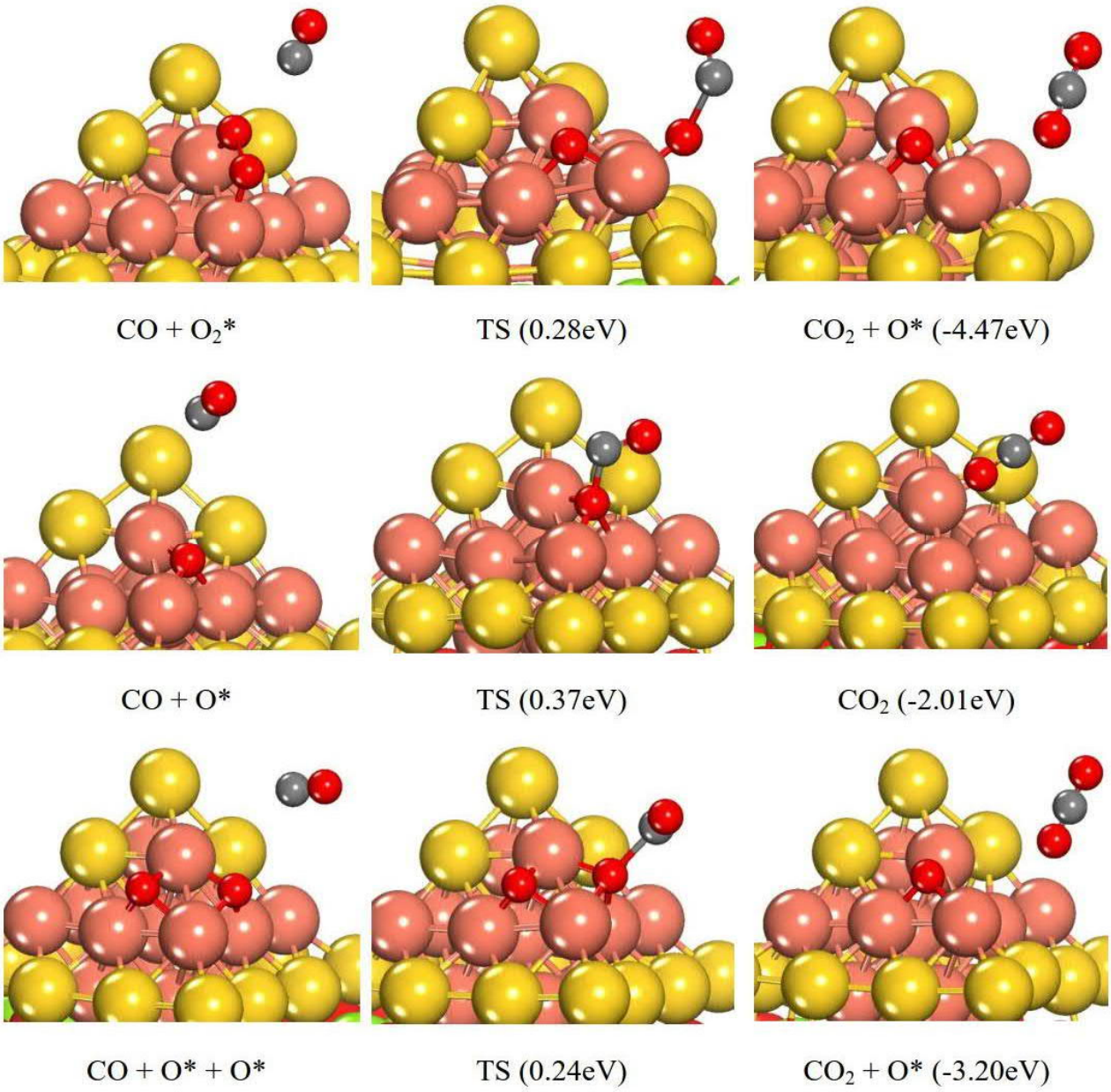

Figure S8 Structures of the initial state (IS), transition state (TS), and final state (FS) for the catalytic CO oxidation on $Au_{15}Cu_{15}$/MgO(100) with the V-center surface by Eley–Rideal (ER) mechanism and the energy changes with respect to the IS. The symbol '*' refers to the atom or molecule being adsorbed on the $Au_{15}Cu_{15}$ cluster.